



HAL
open science

Mg²⁺-dependent conformational equilibria in CorA and an integrated view on transport regulation

Nicolai Tidemand Johansen, Marta Bonaccorsi, Tone Bengtsen, Andreas Haahr Larsen, Frederik Grøn­bæk Tidemand, Martin Cramer Pedersen, Pie Huda, Jens Berndtsson, Tamim Darwish, Nageshewar Rao Yepuri, et al.

► To cite this version:

Nicolai Tidemand Johansen, Marta Bonaccorsi, Tone Bengtsen, Andreas Haahr Larsen, Frederik Grøn­bæk Tidemand, et al.. Mg²⁺-dependent conformational equilibria in CorA and an integrated view on transport regulation. eLife, 2022, 11, 10.7554/eLife.71887 . hal-03853045v2

HAL Id: hal-03853045

<https://hal.science/hal-03853045v2>

Submitted on 15 Nov 2022

HAL is a multi-disciplinary open access archive for the deposit and dissemination of scientific research documents, whether they are published or not. The documents may come from teaching and research institutions in France or abroad, or from public or private research centers.

L'archive ouverte pluridisciplinaire **HAL**, est destinée au dépôt et à la diffusion de documents scientifiques de niveau recherche, publiés ou non, émanant des établissements d'enseignement et de recherche français ou étrangers, des laboratoires publics ou privés.

Mg²⁺-dependent conformational equilibria in CorA and an integrated view on transport regulation

Nicolai Tidemand Johansen^{1†}, Marta Bonaccorsi^{2†}, Tone Bengtsen^{3,4†}, Andreas Haahr Larsen^{1,4}, Frederik Grønbæk Tidemand¹, Martin Cramer Pedersen¹, Pie Huda⁵, Jens Berndtsson⁶, Tamim Darwish⁷, Nageshewar Rao Yepuri⁷, Anne Martel⁸, Thomas Günther Pomorski^{9,10}, Andrea Bertarello², Mark Sansom⁴, Mikaela Rapp⁶, Ramon Crehuet^{3,11}, Tobias Schubeis^{2*}, Kresten Lindorff-Larsen^{3*}, Guido Pintacuda^{2*}, Lise Arleth^{1*}

¹Condensed Matter Physics, Niels Bohr Institute, University of Copenhagen, Copenhagen, Denmark; ²Centre de RMN à Très hauts Champs de Lyon (UMR 5280, CNRS / Ecole Normale Supérieure de Lyon / Université Claude Bernard Lyon 1), University of Lyon, Villeurbanne, France; ³Structural Biology and NMR Laboratory and Linderstrøm-Lang Centre for Protein Science, Department of Biology, University of Copenhagen, Copenhagen, Denmark; ⁴Department of Biochemistry, University of Oxford, Oxford, United Kingdom; ⁵Australian Institute for Bioengineering and Nanotechnology, The University of Queensland, Brisbane, Australia; ⁶Department of Biochemistry and Biophysics, Center for Biomembrane Research, Stockholm University, Stockholm, Sweden; ⁷National Deuteration Facility, Australian Nuclear Science and Technology Organization, Lucas Heights, Australia; ⁸Institut Laue-Langevin, Grenoble, France; ⁹Section for Transport Biology, Department of Plant and Environmental Sciences, University of Copenhagen, Frederiksberg, Denmark; ¹⁰Department of Molecular Biochemistry, Faculty of Chemistry and Biochemistry, Ruhr University, Bochum, Germany; ¹¹CSIC-Institute for Advanced Chemistry of Catalonia (IQAC), Barcelona, Spain

***For correspondence:**

tobias.schubeis@ens-lyon.fr (TS);
lindorff@bio.ku.dk (KL-L);
guido.pintacuda@ens-lyon.fr
(GP);
arleth@nbi.ku.dk (LA)

[†]These authors contributed equally to this work

Competing interest: The authors declare that no competing interests exist.

Funding: See page 16

Received: 02 July 2021

Preprinted: 21 August 2021

Accepted: 04 February 2022

Published: 07 February 2022

Reviewing Editor: Lewis E Kay, University of Toronto, Canada

© Copyright Johansen *et al.* This article is distributed under the terms of the [Creative Commons Attribution License](https://creativecommons.org/licenses/by/4.0/), which permits unrestricted use and redistribution provided that the original author and source are credited.

Abstract The CorA family of proteins regulates the homeostasis of divalent metal ions in many bacteria, archaea, and eukaryotic mitochondria, making it an important target in the investigation of the mechanisms of transport and its functional regulation. Although numerous structures of open and closed channels are now available for the CorA family, the mechanism of the transport regulation remains elusive. Here, we investigated the conformational distribution and associated dynamic behaviour of the pentameric Mg²⁺ channel CorA at room temperature using small-angle neutron scattering (SANS) in combination with molecular dynamics (MD) simulations and solid-state nuclear magnetic resonance spectroscopy (NMR). We find that neither the Mg²⁺-bound closed structure nor the Mg²⁺-free open forms are sufficient to explain the average conformation of CorA. Our data support the presence of conformational equilibria between multiple states, and we further find a variation in the behaviour of the backbone dynamics with and without Mg²⁺. We propose that CorA must be in a dynamic equilibrium between different non-conducting states, both symmetric and asymmetric, regardless of bound Mg²⁺ but that conducting states become more populated in Mg²⁺-free conditions. These properties are regulated by backbone dynamics and are key to understanding the functional regulation of CorA.

Introduction

Magnesium is the most abundant divalent cation (Mg^{2+}) inside the cell, where it is mainly associated with the biological energy source adenosine triphosphate and other negatively charged molecules (Jahnen-Dechent and Ketteler, 2012). Mg^{2+} serves several biological functions, for example as co-factor for enzymes (Jahnen-Dechent and Ketteler, 2012), and Mg^{2+} deficiency is linked to severe diseases including cardiac syndromes, muscular dysfunction and bone wasting (Rude, 1998; de Baaij et al., 2015; DiNicolantonio et al., 2018). CorA is the main ion channel for Mg^{2+} -import in most bacteria and archaea (Maguire, 2006). Despite little sequence conservation, CorA shares two membrane spanning helices and a conserved GMN motif with eukaryotic homologs, including Mrs2 that is responsible for Mg^{2+} -import to the mitochondrial lumen and is essential for cell survival (Papp-Wallace and Maguire, 2007; Knoop et al., 2005).

Several structures determined by X-ray crystallography are available for *Thermotoga maritima* CorA (TmCorA) (Lunin et al., 2006; Eshaghi et al., 2006; Payandeh and Pai, 2006; Nordin et al., 2013; Pfoh et al., 2012). All wild-type proteins have been crystallized as nearly symmetric pentamers in the presence of divalent metal ions and all represent a non-conducting state of the channel with a narrow and hydrophobic pore. Figure 1A shows a representative structure, which is characterized by a transmembrane domain (TMD) connected to the intracellular domain (ICD) by a long stalk helix. The periplasmic entrance to the pore contains the conserved GMN motif that presumably binds to Mg^{2+} via its first hydration shell and thereby acts as a selectivity filter (Nordin et al., 2013; Palombo et al., 2013; Dalmas et al., 2014a). The ICD contains ten inter-protomer binding sites for Mg^{2+} (two per protomer, denoted M1 and M2) involved in regulating the channel (Nordin et al., 2013; Payandeh et al., 2008; Dalmas et al., 2014b). The open state(s) of CorA have so far not been crystallized, but several biochemical and structural studies (Payandeh et al., 2008; Dalmas et al., 2014b) as well as molecular dynamics simulations (Pfoh et al., 2012) have pinpointed the determining residues involved in gating and suggested open models. One model suggests pore dilation upon loss of Mg^{2+} at the M1 (and M2) sites due to a concerted iris-like movement (Dalmas et al., 2014b; Chakrabarti et al., 2010), while another suggests a hydrophobic-to-polar transition of the pore upon concerted rotation of the stalk helices (Guskov et al., 2012; Kowitz and Maguire, 2019).

Recently, cryo-EM structures were obtained both in the presence and absence of Mg^{2+} (Matthies et al., 2016). The Mg^{2+} -bound structure at ~ 3.8 Å resolution was symmetric and closed, in line with crystal structures, whereas two Mg^{2+} -free structures at ~ 7.1 Å were symmetry broken and with dilated pores. Figure 1B shows an intracellular view of the symmetric and asymmetric states, highlighting the symmetry break upon removing Mg^{2+} . From these observations, the proposed model involves a sequential destabilisation of CorA upon Mg^{2+} removal, leading to a highly dynamic protein with shuffling protomers in the ICD, increasing the likelihood of pore dilation and wetting events (Matthies et al., 2016; Neale et al., 2015). Recent coarse-grained MD simulations revealed the residue level

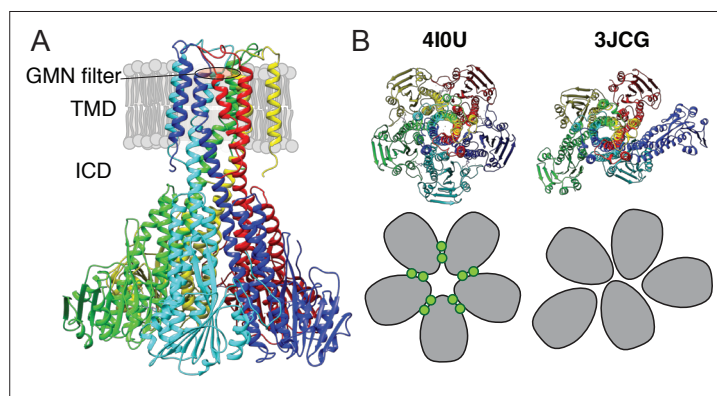


Figure 1. X-ray and cryo-EM structures of CorA. (A) Side view of symmetric CorA (PDB ID: 410U) in presence of Mg^{2+} ('closed form'). (B) Top view of the same symmetric state of CorA (PDB ID: 410U) side-by-side to one of the asymmetric states observed in the absence of Mg^{2+} ('open form') (PDB ID: 3JCG). A schematic representation of the two forms is shown below their structures, with each monomer shown in gray and Mg^{2+} ions represented as green circles.

details of how a complex interaction network involving asymmetric movements of ICD monomers ultimately led to a conducting state upon removal of Mg^{2+} (Nemchinova et al., 2021). High-speed atomic force microscopy (HS-AFM) data on densely packed CorA in lipid bilayers supported this model, but at the same time provided more insight to the dynamic interconversion of different states, including a fourth population of highly asymmetric CorA, not resolved by cryo-EM (Rangl et al., 2019). Interestingly, this population accounted for most observed conformations at low Mg^{2+} concentrations, supporting that CorA is a dynamic protein with a relatively flat energy landscape and, potentially, multiple open states. However, CorA mutants with mutated regulatory M1 sites were still able to crystallize in the (symmetric) closed state (Kowatz and Maguire, 2019), suggesting that inter-protomer binding of Mg^{2+} is not required for closing the channel. Overall, the cryo-EM and AFM experiments hint towards a highly dynamic ensemble of primarily asymmetric states at low Mg^{2+} concentrations, while the successful crystallisation of M1 site mutants suggests that the closed state is significantly present at these conditions.

In this study, we investigated CorA using two room-temperature methods, namely small-angle neutron scattering (SANS), sensitive to large amplitude conformational changes and magic-angle spinning solid-state NMR (MAS NMR), sensitive to structure and dynamics with atomic resolution (Reif et al., 2021; Bonaccorsi et al., 2021). For both methods, we employ custom-developed state-of-the-art methodology, that is size-exclusion chromatography (SEC) coupled to SANS (Johansen et al., 2018; Jordan et al., 2016) and match-out deuterated carrier systems for SANS (Maric et al., 2014; Midtgaard et al., 2018) (so-called stealth carrier systems), and >100 kHz MAS NMR in lipid bilayers (Schubeis et al., 2018; Schubeis et al., 2020). Based on these data in conjunction with molecular simulations and modelling, we propose a model in which CorA is in a dynamic equilibrium between symmetric and asymmetric states, independent of bound Mg^{2+} , but where an ensemble of conducting states is energetically more favourable for Mg^{2+} -free CorA due to increased conformational dynamics resulting from the released electrostatic constraint.

Results

CorA is structurally similar in presence and absence of Mg^{2+}

The published cryo-EM structures of CorA in absence of Mg^{2+} (Figure 1B, 3JCG) reveal large structural rearrangements compared to the nearly symmetric, non-conductive state obtained from crystallography (Figure 1B, 4I0U). SANS curves calculated from these two structural states of CorA reveal a significant change in the scattering curve in the region $q = 0.08 \text{ \AA}^{-1} - 0.15 \text{ \AA}^{-1}$ (Figure 2A and B, right panels), that is on a length scale that is well-covered in a standard SANS experiment. To match the cryo-EM conditions, we performed SANS measurements in n-dodecyl-B-D-maltoside (DDM) detergent micelles and 2-Oleoyl-1-palmitoyl-sn-glycero-3-phosphocholine (POPC) lipid nanodiscs. We used selectively deuterated versions of both carrier types that were homogeneously matched-out and hence invisible at 100% D_2O ; that is stealth DDM (sDDM) and stealth nanodiscs (sND, Figure 2—figure supplement 1). Strikingly, the measured SANS curves are pair-wise indistinguishable in the absence of Mg^{2+} (1 mM EDTA) and in the presence of 40 mM Mg^{2+} for the sDDM (Figure 2A) and sND (Figure 2B) samples, respectively, indicating no significant difference in the average conformations of the Mg^{2+} -free and bound states of CorA. This observation contrasts with the recently proposed large-scale structural rearrangements reported from cryo-EM and high-speed AFM data.

We note that the SANS data obtained on the sND samples (Figure 2B) have a slight excess scattering contribution at low- q compared to the sDDM samples (Figure 2A), which can be attributed to the presence of a few *E. coli* endogenous lipids in the sND samples. However, the SANS data from sDDM and sND samples are indistinguishable in the q -region expected to reveal differences from symmetric and asymmetric states (Figure 2—figure supplement 2), which confirms that CorA exhibits the same behaviour in a POPC lipid environment and in DDM detergent carriers. The rightmost panels of Figure 2A and B show enhanced views on this region for the SANS data compared to the SANS curves calculated from the PDB structures. Interestingly, neither of the curves calculated from the PDB structures match the measured SANS data, suggesting that the solution structure of CorA cannot be described by any of these single structures, regardless of whether or not CorA is in the presence of Mg^{2+} .

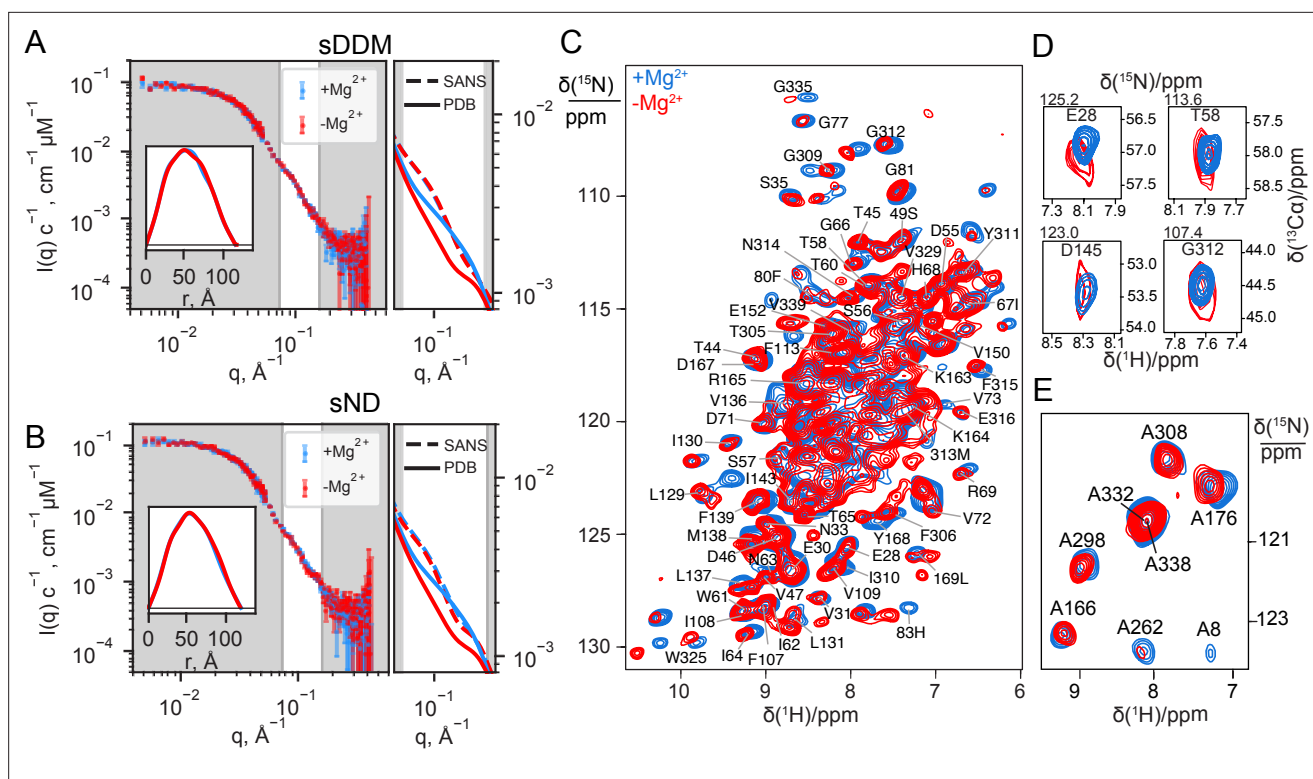


Figure 2. Experimental data on CorA in presence (blue) and absence (red) of Mg^{2+} . **(A + B)** Experimental SANS data of CorA embedded in stealth DDM micelles (sDDM) and stealth nanodiscs (sND), respectively, with $p(r)$ -distributions calculated on BayesApp (Hansen, 2014) in the inset. The rightmost plots show zoomed comparisons of the $p(r)$ -fits of experimental data (SANS, dashed lines) with the SANS curves calculated on the X-ray (4IUO) and cryo-EM (3JCG) structures (PDB, full lines). Complete fits based on the PDB structures are shown in Figure 4A. **(C)** 2D 1H - ^{15}N dipolar correlation spectra by MAS NMR of CorA in hydrated DMPC bilayers recorded at 1 GHz 1H Larmor frequency and 107 kHz MAS. **(D)** 2D sections for a selection of residues obtained from 3D 1H - ^{15}N - $^{13}C\alpha$ spectra recorded at 1 GHz 1H Larmor frequency and 107 kHz MAS. **(E)** 2D 1H - ^{15}N dipolar correlation spectra obtained for ^{15}N -Alanine-labeled CorA recorded at 1 GHz 1H Larmor frequency and 60 kHz MAS. In C and E, site-specific assignments are annotated for resolved resonances.

The online version of this article includes the following figure supplement(s) for figure 2:

Figure supplement 1. Validation of nanodisc match-out deuteration.

Figure supplement 2. Comparison of SANS data in sDDM and sND.

Figure supplement 3. Absolute chemical shift differences in 3D 1H - ^{15}N - $^{13}C\alpha$ spectra of CorA with and without Mg^{2+} , calculated as $\Delta(\delta) = \sqrt{(\delta_{X,+Mg} - \delta_{X,-Mg})^2}$ for $X=^1H, ^{13}C\alpha, ^{15}N$.

While SANS data provided information on the overall molecular shape of CorA in the two preparations, we used MAS NMR to obtain insight into structural changes at the residue-level length-scale. MAS NMR data were recorded on uniformly ^{13}C , ^{15}N -labelled CorA, reconstituted in 1,2-dimyristoyl-sn-glycero-3-phosphocholine (DMPC) lipid bilayers, in the presence or absence of Mg^{2+} . Backbone resonance assignment was obtained at high Mg^{2+} concentration acquiring a set of three-dimensional experiments relying on $^1H^N$ and $^1H\alpha$ detection with 100 kHz MAS. We were able to annotate ~100 peaks to residues spread throughout the structure of CorA. Notably, the assignment of CorA with and without Mg^{2+} is clustered in the globular region in the ICD and in the TMD, including the important periplasmic loop, whereas only sparse assignments were established in the long portion (243-289) of the stalk helix connecting the two regions. The determination of random coil chemical shift deviation (CSD) values confirmed that the secondary structure is in good agreement with the one obtained by X-ray crystallography and Cryo-EM.

2D 1H - ^{15}N dipolar correlation spectra represent direct structural ‘fingerprints’ of CorA in the two preparations. Despite the high signal overlap associated to the high-molecular-weight of CorA, fast MAS rates and the ultra-high magnetic field guarantee high sensitivity and feature numerous signals with a resolution sufficient to track subtle structural changes. Once again, against our expectations,

we remarked that the spectra with and without Mg^{2+} showed very little difference, with the positions of the resolved peaks differing less than 0.1 ppm in the two forms and without peak splitting or broadening that would indicate distinct conformations (Figure 2C).

Two parallel strategies were pursued to extend the analysis to the more crowded regions. First, we acquired three-dimensional (3D) experiments which correlate the amide proton and nitrogen with the C_{α} -carbon within each residue and thus include an additional ^{13}C chemical shift dimension (Figure 2D). The resulting 3D spectra confirmed negligible chemical shift variations over more than ~90 sites across the TMD and ICD (Figure 2D, Figure 2—figure supplement 3). In the Mg^{2+} -free sample, however, a notable decrease in signal intensity was observed for most residues, resulting in the complete disappearance of two thirds of the peaks from the TMD (vide infra).

Secondly, we used amino-acid-specific isotopic enrichment to select the NMR signals associated to the amide groups of the alanine residues. Each CorA protomer contains eight alanine residues, distributed with four in the TMD and four in the ICD, which were all visible and assigned in the corresponding 1H - ^{15}N dipolar correlation spectra of two preparations with and without magnesium (Figure 2E). Also, in this case, the spectra are superimposable and show no evidence of peak splitting.

In conclusion, and in line with SANS, the NMR data show that the predominant structure of CorA in lipid bilayers is unaltered by the removal of Mg^{2+} .

CorA is active and preserves its tertiary structure in D_2O

Since Mg^{2+} hydration plays an important role in CorA selectivity, and D_2O and H_2O have slightly different physicochemical properties (Némethy and Scheraga, 1964), we speculated whether the identical SANS curves with and without Mg^{2+} were due to CorA losing its activity in the SANS condition, that is at 100% D_2O . To test this, we measured the activity of CorA in POPC liposomes under the SANS conditions by a fluorometric assay (Figure 3A). This analysis shows that CorA is clearly active in D_2O . The transport rate estimated from the initial linear part of the trace is lower by less than a factor of two compared to H_2O . A slightly reduced rate in D_2O has been reported for other membrane proteins (Sugiyama and Yoshiok, 2012) and is explainable by slightly altered properties of the two solvents (Némethy and Scheraga, 1964; Hummer et al., 2000). We could also inhibit CorA activity in D_2O with $Co[NH_3]_6^{3+}$ (Figure 3A, green), supporting that the protein is indeed functional under the SANS conditions.

We further carried out negative stain EM on samples of CorA in DDM and D_2O with or without Mg^{2+} . The refined 2D classes clearly show that the pentameric architecture of CorA is preserved in D_2O in both conditions (Figure 3B). Furthermore, several 2D classes appear to exhibit approximate fivefold

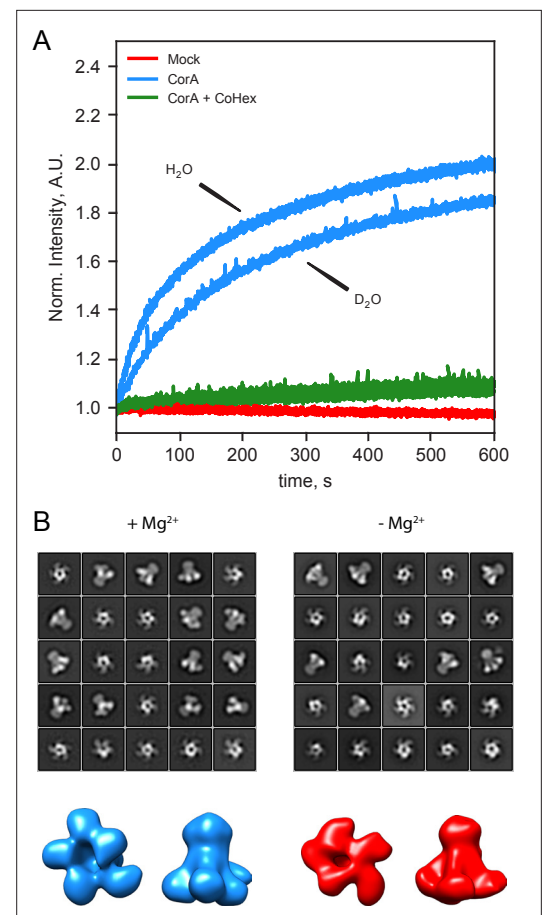


Figure 3. CorA activity in D_2O and direct visualization by negative stain EM. (A) CorA activity in the conditions used for SANS. The traces are the normalized fluorescence signals after adding Mg^{2+} to either empty POPC liposomes (Mock), CorA-POPC proteoliposomes (CorA), or CorA-POPC proteoliposomes preincubated with the inhibitor $Co[NH_3]_6^{3+}$ in D_2O (CorA+ CoHex). (B) Negative stain EM of CorA in DDM and D_2O with and without Mg^{2+} . The 25 most abundant 2D classes are shown for each condition. The box dimensions are $170 \times 170 \text{ \AA}^2$ for scale. (C) Final 3D model for each condition shown from the intracellular side and in side-view, respectively.

symmetry, both in the presence and absence of Mg^{2+} . To avoid bias, we refined 3D models without imposing symmetry (**Figure 3C**). In both conditions, these low-resolution 3D models ($\approx 15 \text{ \AA}$) are reminiscent of the overall expected architecture of CorA (**Figure 1**), but notably show some degree of asymmetry. In conclusion, CorA show little to no perturbation from measurements in D_2O , rendering the SANS data sets viable for modelling of the solution structure of CorA.

Model refinement to SANS data shows that CorA is asymmetric

The SANS data sets obtained in sDDM (**Figure 2A**) exhibit well-defined Guinier-regions and the calculated radii of gyration, R_g , of $42.1 \pm 1.3 \text{ \AA}$ (+ Mg^{2+}) and $43.8 \pm 1.7 \text{ \AA}$ (- Mg^{2+}) are close to the predicted values from the X-ray (41.3 \AA) and cryo-EM structures (42.2 \AA and 42.3 \AA). Thus, these data are indicative of well-separated CorA pentamers with no interference from visible lipids or the kind, providing the optimal basis for structural modelling. Given the high similarity of the SANS data obtained on the samples of CorA in sDDM with and without Mg^{2+} , we performed structural modelling on only a single data set, that is CorA in sDDM without Mg^{2+} (**Figure 2A**, red). Despite controversies on the open state, there is consensus that the crystallized symmetric state represents the closed state of the protein. Surprisingly, we could not obtain good fits of the symmetric state to our SANS data without clear systematic deviations, especially at the feature present at $q \approx 0.1 \text{ \AA}^{-1}$ (**Figure 4A**, 410U). This was also the case for the asymmetric cryo-EM structure (**Figure 4A**, 3JCG) that produced an even worse fit. In SANS, the signal represents a population-weighted average of all conformations that the protein can adopt. With a measurement time on the order of several minutes and illumination of $\approx 10^{12}$ – 10^{13} molecules, all accessible populations are expected to contribute to the signal. A relatively flat energy landscape with multiple interconverting states has been proposed in Mg^{2+} -free conditions, making a fit of a single structure less meaningful in this context. However, it is unlikely that the average of an ensemble of asymmetric structures give rise to the same SANS signal as that of a single symmetric state corresponding to the structure determined by crystallography and cryo-EM in high Mg^{2+} .

With no scattering contribution from the carrier systems, it becomes possible to analyse the SANS data by conventional methods for soluble proteins, such as bead-modelling. When imposing P5 symmetry, we could obtain envelopes reminiscent of the CorA structure by bead-modelling (**Figure 4—figure supplement 1B**), whereas no symmetry (P1) imposed led to asymmetric mass distributions that were not at all compatible with the overall architecture of CorA (**Figure 4—figure supplement 1A**). This indicates that there is significant structural dispersion in the sample.

To obtain a molecular constrained model compatible with the data, we applied a modified type of normal mode analysis (NMA), starting from the closed crystal structure. A structure with mostly intact secondary structure but a high degree of asymmetry in the ICDs yielded a good fit to the SANS data (**Figure 4B**). Importantly, this model describes the feature at $q \approx 0.1 \text{ \AA}^{-1}$, where the PDB models deviate the most. Thus, on average, the solution structure of CorA appears to be asymmetric, in line with our EM models (**Figure 3C**). Again, we emphasize that such an overall asymmetric structure of CorA in presence of excess Mg^{2+} is in stark contrast to the picture of a closed, symmetric structure that has served the basis for all proposed mechanisms of Mg^{2+} gating. However, a single asymmetric model as derived from NMA (**Figure 4B**) is neither compatible with a single set of peaks in NMR (**Figure 2C and E**) nor the substantial experimental evidence for a nearly symmetric, closed state in presence of Mg^{2+} . Likely, CorA adopts multiple different states (**Matthies et al., 2016; Rangl et al., 2019**), and according to our data does so both with and without Mg^{2+} bound. In this case, the SANS data would represent the number-weighted average of different states that must be overall asymmetric.

To model the apparent asymmetry in CorA in more detail and as a conformational ensemble, we performed coarse grained molecular dynamics simulations (MD). First, we set up CorA embedded in a POPC bilayer using the Martini3.0b force field. Starting from the symmetric or asymmetric structures, 32 μs and 20 μs simulations, respectively, without any inter-chain elastic network terms yielded only small structural fluctuations, which did not significantly improve fits to the experimental SANS data, especially not around the feature at $q \approx 0.1 \text{ \AA}^{-1}$. Thus, we extended the analysis to metadynamics simulations (MetaD) that allows for enhanced sampling of structural dynamics. MetaD drives the simulation towards a larger variety of structural states based on an energetic bias on a structural feature, a so-called collective variable, here the R_g on specific ICD residues. Starting from the symmetric structure, the MetaD simulation quickly drove the simulation away from the local structural minimum that

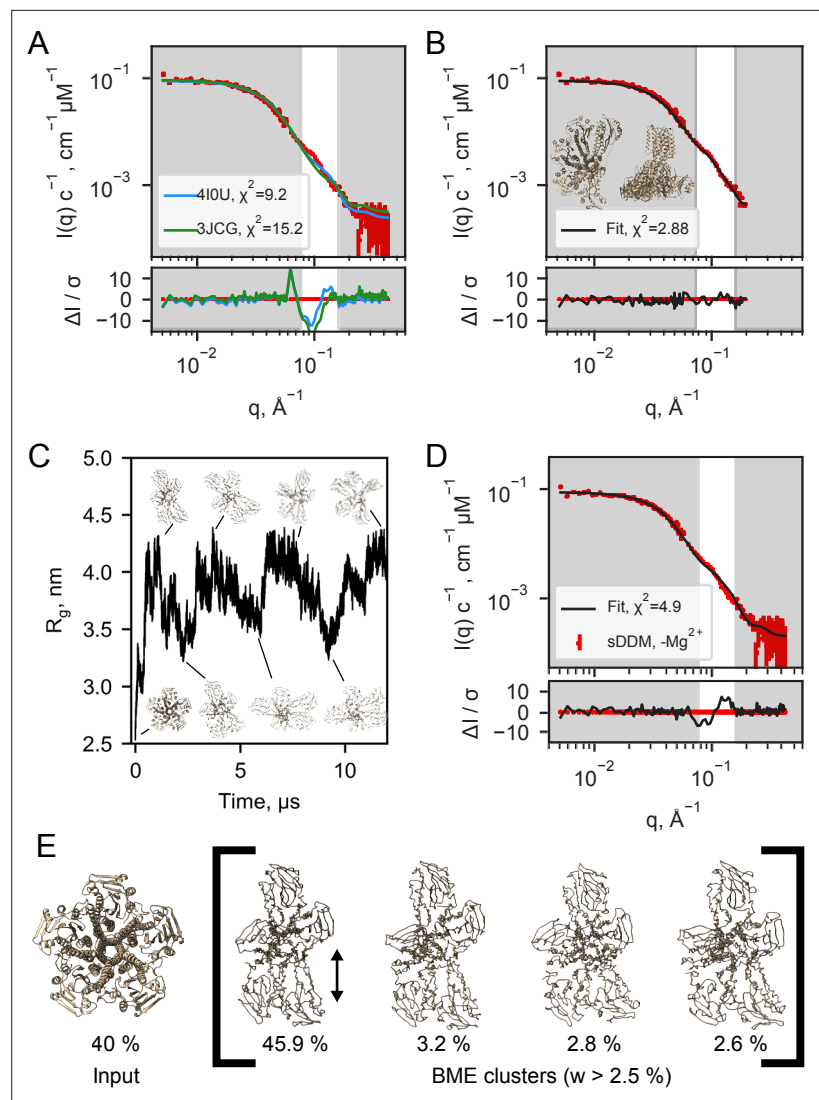


Figure 4. Structural modelling of CorA from SANS data. **(A)** Model fits of the closed crystal structure (410U) and open cryo-EM structure (3JCG) to the experimental SANS data obtained in sDDM without Mg^{2+} . The bottom panel shows the error-normalised difference plot of the fits. **(B)** Model fit of the structure obtained by regularised normal mode analysis (bottom and side views inserted on plot). **(C)** MetaD molecular dynamics trajectory with representative frames visualized as ribbon structures. **(D)** Fit of a weighted ensemble obtained from the MD simulation in B together with a 40% contribution from the symmetric CorA. **(E)** The four highest weighted cluster centroids in the metaD simulation (right bracket) together with the closed symmetric structure (left) which together illustrates the ensemble of CorA structures that produced the best fit to the experimental SANS data.

The online version of this article includes the following figure supplement(s) for figure 4:

Figure supplement 1. Bead modelling of CorA.

Figure supplement 2. Goodness of fit from NMA generated structures to SANS.

Figure supplement 3. Ensemble fitting to SANS data with symmetric CorA included.

Figure supplement 4. Representation of the pore radius profile in the transmembrane domain obtained by HOLE program out of the structures calculated by Normal Mode Analysis and MetaDynamics.

the standard MD had been trapped in and sampled a large range of conformationally different structures (**Figure 4C**).

The averaged back-calculated SANS of the entire ensemble of structures obtained from MetaD simulations did not fit the experimental SANS data satisfactorily. This can be explained by for example remaining inaccuracies in the coarse grained force field and imprecisions in the simulation

from insufficient sampling. To resolve this, we applied the Bayesian/Maximum Entropy reweighting method (BME) to optimize the weights of the individual conformations in the simulation with the aim of obtaining an ensemble in better agreement with the experimental SANS data. In addition to the BME, we enforced that a symmetric state should be present in the final ensemble, given the substantial experimental evidence for this state in the literature and that it was under-sampled in the simulation. The best fit to the SANS data (**Figure 4D**) was obtained with an ensemble consisting of $40\% \pm 28\%$ symmetric CorA structure and the remainder of asymmetric conformations from the MetaD (**Figure 4E** and **Figure 4—figure supplement 3**). Despite some systematic deviations, the fit is much improved with regards to describing the feature in the SANS data at $q \approx 0.1 \text{ \AA}^{-1}$, as compared to the fits obtained with the symmetric crystal structure or the open cryo-EM structures, respectively (**Figure 4A**).

To visualise the results of the MetaD simulation and hence the simulated dynamics, we cluster similar structures and show the four most predominant cluster centroids (**Figure 4E**) where especially one cluster contributes to the final fitted ensemble. Although the four cluster centroids are wide apart in simulation time ($\approx 500 \text{ ns}$), they are structurally similar with a maximum pairwise RMSD of 6.5 \AA (data not shown). The main difference is the distance between the two protomers (**Figure 4E**, black arrow), which indicates that the individual domains of the ICD can move relative to each other. This is in line with the subunit displacements described in the symmetry-break-based gating model derived from the cryo-EM structures and supported by AFM measurements. Importantly, however, we find that these movements occur irrespective of the presence of Mg^{2+} , given the nearly identical SANS data in the two conditions.

To investigate whether asymmetric transitions correspond to an opening of the channel, we analysed critical distances between protomers within the NMA- and metaD-generated structures. In the asymmetric structures refined from MetaD simulations, only a single binding site in the cytoplasmic region remains competent to coordinate Mg^{2+} , whereas in the NMA-generated structure, four binding sites remain within distance to bind Mg^{2+} . In the transmembrane region, the pore dimensions obtained by the HOLE program (*Smart et al., 1996*) indicate that for all the NMA- and MetaD-generated structures, the pores contain narrow constrictions with diameters significantly smaller than the 2.4 \AA radius of hydrated Mg^{2+} (*Maguire and Cowan, 2002, Figure 4—figure supplement 4*). This suggests that all the refined asymmetric structures are in fact non-conducting. Taken together, the general picture of our simulations does not provide a mechanistic link between symmetry break and channel-opening. On the other hand, this suggests that symmetry-break alone is not sufficient for obtaining ion transport.

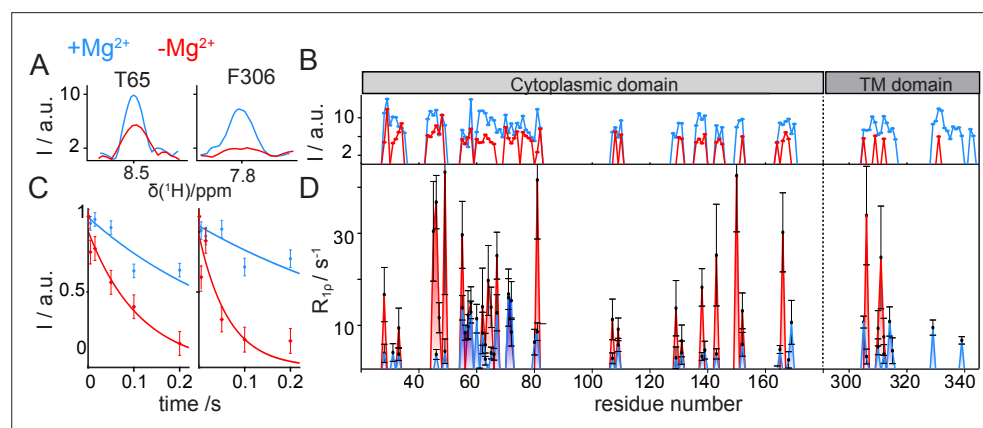


Figure 5. CorA backbone dynamics by MAS NMR in DMPC in presence (blue) and in absence (red) of Mg^{2+} . (A) Examples of 1D traces of 3D ^1H - ^{15}N - $^{13}\text{C}\alpha$ peaks for two residues in the ICD (T65) and in the TMD (F306). (B) Comparison of peak intensities in 3D ^1H - ^{15}N - $^{13}\text{C}\alpha$ spectra over the protein sequence. ICD and TMD are indicated by boxes of different color on top of the plot. C-D: Site-specific ^{15}N $R_{1\rho}$ rates measured with a 15 kHz spin-lock field. (C) Examples of ^{15}N $R_{1\rho}$ relaxation decays together with the corresponding mono-exponential fits for residues T65 and F306. (D) Comparison of site-specific backbone ^{15}N $R_{1\rho}$ rates plotted along the CorA sequence.

The online version of this article includes the following figure supplement(s) for figure 5:

Figure supplement 1. CorA backbone dynamics by MAS NMR: Site-specificity and temperature dependence.

Structural dynamics are different in open and closed states of CorA

So far, we have considered a set of static snapshots to interpret the wide variety of populated states of CorA. The observation of MAS NMR dynamical probes sheds light on the backbone motions of these states over different timescales, enriching the structural description of CorA with conformational plasticity. A first insight on site-specific dynamics is obtained by comparing the peak intensities observed in the MAS NMR experiments in the two samples with and without Mg^{2+} . Peak intensities are dependent on dipolar couplings between nearby nuclei and are affected when such couplings are averaged by local motions. For an amide ^1H - ^{15}N pair, this corresponds to motional processes faster than tens of kHz (i.e. more rapid than hundreds of μs).

Changes in peak intensity are already noticeable in the 2D ^1H - ^{15}N dipolar correlation spectra, but are amplified in the 3D correlations, where additional radio-frequency irradiation periods act as a more stringent filter, dumping the signals of the most mobile sites. 1D traces of two exemplar 3D ^1H - ^{15}N - $^{13}\text{C}\alpha$ correlations (T65 in the ICD and F306 in the TMD) and the plot of signal intensities over the full protein sequence with and without Mg^{2+} are shown in **Figure 5A and B**, respectively. As mentioned above, an overall decrease in peak intensities is associated to removal of Mg^{2+} , with a stronger effect observed in the TMD. This points toward a variation of the dynamic behavior of this region in the two samples.

^{15}N spin-lattice relaxation rates in the presence of a spin-lock field (^{15}N $R_{1\rho}$) are sensitive reporters of motions occurring over a window of hundreds of ns to hundreds of μs . These parameters were measured site-specifically for ~ 40 residues in the CorA backbone, by introducing a relaxation filter in the ^1H - ^{15}N dipolar correlation module and monitoring the signal decay of each amide pairs in a series of experiments with increasing relaxation delays (**Figure 5C**). Despite the intrinsically low signal-to-noise ratio of the experiments, which results in very large uncertainties on the site-specific relaxation rates, a remarkable (up to 10 fold) systematic increase was observed throughout the entire protein upon removal of Mg^{2+} (**Figure 5D**). The same effect was observed for the ^{15}N -alanine labelled sample (**Figure 5—figure supplement 1A**). An additional measurement of ^{15}N $R_{1\rho}$ rates upon a $\sim 20^\circ\text{C}$ cooling revealed a different temperature-dependent behaviour of the two Mg^{2+} -loaded samples (**Figure 5—figure supplement 1B**). While in the presence of Mg^{2+} relaxation rates were conserved at low temperatures, an important (2–3 fold) decrease was observed in the Mg^{2+} -free form. Finally, also dynamics on the ns timescale obtained by the measurements of bulk backbone ^{15}N R_1 showed a global increase of relaxation rates (by a factor ~ 1.5) upon removal of Mg^{2+} (**Figure 5—figure supplement 1C**).

In summary, MAS NMR reveals that removal of Mg^{2+} triggers an increase in the backbone flexibility on different timescales, a dynamical effect which is different for the ICD and the TMD.

Discussion

The functional mechanism of the pentameric divalent cation channel CorA of *Thermotoga maritima* has been under investigation since the release of the first high-resolution structures in 2006. The gating mechanism is most commonly explained by a simple two-state model, involving a conformational transition between a closed symmetric state and one or many open asymmetric states. Indeed, the concise current model derived from cryo-EM (**Matthies et al., 2016**) and HS-AFM (**Rangl et al., 2019**) defines a rigid symmetric conformation at high Mg^{2+} concentrations (> 20 mM), dynamic asymmetric conformations at low Mg^{2+} concentrations (2–3 mM) and several distinct rigid asymmetric conformations in the absence of Mg^{2+} .

We have performed SANS in stealth carrier systems to study the solution conformation of CorA, together with modeling of both static and ensemble structures obtained from MetaD simulations. Furthermore, we used ^1H -detected solid-state NMR to investigate CorA conformation and dynamics in hydrated lipid bilayers. These complementary methods allow us to expand the current view on the mechanistically important conformational equilibria.

Symmetric and asymmetric structures are populated both in the presence and absence of Mg^{2+}

While our SANS data probes the overall solution conformation of CorA at low resolution of around 20 Å, it is important to note that the technique is indeed quite sensitive to structural rearrangements

on much smaller length scales when the same sample, but under different conditions, is compared internally. As such, given the identical SANS data recorded in absence and presence of high Mg^{2+} concentrations, we conclude that the overall solution structure of CorA is similar in both conditions. Our refinement of models to the SANS data shows that CorA is overall asymmetric, contradicting the idea of a single rigid, symmetric structure in high Mg^{2+} concentrations. Indeed, our data can only be explained by symmetry breaking and/or a mixture of populations, for example through the concomitant presence of symmetric and asymmetric states. Furthermore, NMR spectra are sensitive to the environments of each nucleus, and thus report on conformational transitions breaking the local symmetries. The fact that NMR chemical shifts do not change significantly upon removal of Mg^{2+} indicates the conservation of local symmetric environments for most of the NMR-active nuclei in both conditions. In turn, this evidence suggests that the global symmetry is maintained for a substantial population of CorA pentamers in the absence of Mg^{2+} . Hence, we have from SANS that symmetry breaking is present at both high and low Mg^{2+} , and from NMR that a substantial population of CorA is on the symmetric form in both Mg^{2+} conditions. These findings are supported by our negative-stain TEM data, but also by the literature. For example, the symmetric cryo-EM structure (3JCF) obtained at high Mg^{2+} concentrations, resulted from roughly 60% of the particles (Matthies *et al.*, 2016), which implies that asymmetric states could partly account for the remaining 40%. The two asymmetric cryo-EM structures were refined from only about 15% each of the picked particles, indicating the presence of various conformations, and likely including the symmetric form. AFM provided a more detailed conformational analysis and found around 20% symmetric structures at low Mg^{2+} concentrations (0–3 mM) (Rangl *et al.*, 2019).

Increased dynamics of CorA in absence of Mg^{2+}

An elevated conformational plasticity at low levels of Mg^{2+} was first postulated due to the unsuccessful crystallization trials in these conditions. Structural evidence for this arrived with the finding of several asymmetric states on cryo-EM grids and was recently supported by the observation of real time dynamics on a timescale of seconds through high-speed AFM (Rangl *et al.*, 2019). MAS NMR has the exclusive advantages of probing molecular motions with site-specific resolution and the possibility to tune the experiments towards a dynamic timescale of interest. On a fast ps-ns timescale, we observed increased bulk ^{15}N R_1 s in the absence of Mg^{2+} , indicating less restricted backbone motions, as also previously suggested by MD simulations (Chakrabarti *et al.*, 2010). Site-specific ^{15}N R_1 rates

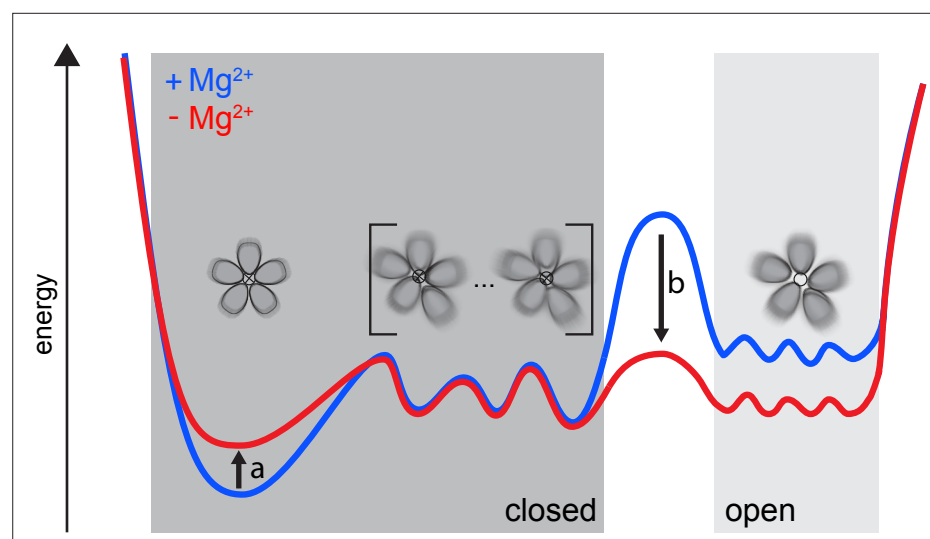


Figure 6. Our proposed dynamic model for CorA. Both in high and low intracellular Mg^{2+} levels, a complex ensemble of closed states (left), symmetric as well as asymmetric, are in equilibrium with an ensemble of open states (right). At high Mg^{2+} (blue) the large energy barrier prevents CorA from visiting the ensemble of open states. At low intracellular Mg^{2+} levels (red) a reduction in the population of the symmetric, closed state (arrow a) is induced. At the same time the energy barrier (arrow b) is lowered toward the ensemble of open states, which then becomes populated.

are reporters of segmental motions, for example displacement of secondary structure elements with respect to each other, over a window of hundreds of ns to hundreds of μ s. These dynamical processes appear to be largely promoted over the whole CorA structure when Mg^{2+} is absent. We also observed that motions in stalk helix 7, already present in the Mg^{2+} -bound sample, propagated into the transmembrane domain when Mg^{2+} was removed. Thus, we can indeed confirm that the dynamics of CorA increase at low Mg^{2+} concentrations, but also that motions occur on various timescales. A previous work suggested that removal of Mg^{2+} resulted in a combination of lateral and radial tilting of two adjacent monomers, which allowed the creation of interactions between them (Pfoh *et al.*, 2012). This idea was recently extended based on coarse-grained MD simulations that showed an ensemble of conformational changes propagating from the ICD to the TMD helices (Nemchinova *et al.*, 2021). In line with these observations, we propose that collective ns- μ s motions of the backbone initially promoted in the ICD by release of Mg^{2+} ions would in turn induce higher conformational flexibility in the TMD. While a detailed understanding of those complex dynamic processes will require elaborate follow-up experiments, we can interpret our current findings in the view of how conformational changes regulate the channel opening.

An integrated view on CorA transport regulation

First, we remark that our findings cannot be explained in terms of sharp transitions between open and closed states. In other words, a high degree of asymmetry is not equivalent to an open state. We propose an alternative model, schematically illustrated in **Figure 6**, that integrates our findings with the previously available literature. CorA samples symmetric and asymmetric conformational states, whose distribution is tuned by the Mg^{2+} concentration. Between the symmetric, closed state and an ensemble of open states, a relatively flat energy landscape exists with asymmetric, closed states, both in the presence and absence of Mg^{2+} . Low Mg^{2+} intracellular levels induce a reduction in the population of the symmetric, closed state together with a decrease of the energy barrier toward an ensemble of open states, which become populated. In this context, increased dynamics, as observed by NMR, can become the key determinant allowing CorA to explore different wells of the energy profile, making the open state reachable.

Such a dynamic model is compatible with previously unexplainable symmetric crystal structures of M1-binding site mutants in the absence of Mg^{2+} (Kowitz and Maguire, 2019). While for WT CorA, removal of Mg^{2+} increases the dynamics and shifts the conformational equilibria, point mutations probably have an opposite effect, stabilizing the symmetric state and allowing crystal formation. Furthermore, this model aligns with a previous MD study, which found that dry and intermediate transiently wetted states, both non-conducting, were present irrespective of bound Mg^{2+} and with interconversion rates on the ns time scale, whereas without Mg^{2+} bound, a conducting 'stably-superhydrated' state was sampled as well (Neale *et al.*, 2015).

Intriguingly, the interplay between symmetric and asymmetric conformations have also been investigated for another family of pentameric channels, the ligand-gated ion channels (pLGIC) (Rao *et al.*, 2021). While these are usually symmetric or pseudo-symmetric in the ligand-free form, studies suggest that asymmetric resting states exist as intermediates in the conformational landscape, and that they become more energetically favorable when substrate is bound (Zhang *et al.*, 2021). As such, it appears that asymmetry might have a more widespread occurrence in channel regulation.

Conclusion

The availability of room temperature SANS and NMR data of CorA in lipid bilayers, reporting on both global and local behaviour of this channel, supported by MD simulations, allowed us to extend and rationalise the 'symmetry-break-upon-gating' model for Mg^{2+} transport. Our observations support the suggestion that asymmetric conformations are involved in the gating mechanism, but in a more complex way than a simpler two-state picture, where Mg^{2+} -bound CorA is a stable, symmetric structure. Indeed, we find that the CorA pentamer is a symmetry-broken fluctuating structure able to explore a wide conformational landscape both in the presence and absence of Mg^{2+} . We propose that the determining factor for CorA to visit conducting states is the increase in backbone flexibility on different timescales upon release of regulatory Mg^{2+} . Future investigations of the conformational equilibria will enrich the insight provided in this study with a better mechanistic understanding of the

kinetics and thermodynamics of gating and transport, and more detailed atomic-resolution simulations may shed light on the ion regulation and transport pathways.

Materials and methods

Key resources table

Reagent type (species) or resource	Designation	Source or reference	Identifiers	Additional information
Gene (<i>Thermotoga maritima</i>)	corA	Uniprot	Q9WZ31	
Strain, strain background (<i>Escherichia coli</i>)	BL21 star(DE3)	ThermoFisher	C601003	
Software, algorithm	PEPSI-SANS	https://team.inria.fr/nano-d/software/pepsi-sans/	RRID:SCR_021950	
Software, algorithm	NOLB	Ref. 48	RRID:SCR_021954	
Software, algorithm	Martini3.0b	Ref. 49	RRID:SCR_021951	
Software, algorithm	GROMACS-5.1.4	Ref. 52	RRID:SCR_014565	
Software, algorithm	PLUMED2.3.0	Ref. 56	RRID:SCR_021952	
Software, algorithm	BME	Ref. 58	RRID:SCR_021953	
Software, algorithm	CcpNmr Analysis	Ref. 64	RRID:SCR_016984	
Software, algorithm	FLYA	Ref. 65	RRID:SCR_014229	

Materials

All chemicals were from Sigma-Aldrich unless otherwise stated. DDM was from Carbosynth (UK), match-out-deuterated DDM (sDDM *Midtgaard et al., 2018*) and match-out deuterated POPC (d-POPC) were synthesised at the National Deuteration Facility at ANSTO (Lucas Heights, Australia). The d-POPC was synthesised as previously (*Yepuri et al., 2016*), but with custom deuteration (94% D in tail groups, 71 %D in head group). Details of the synthesis and chemical and isotopic analysis are described in Appendix 1.

Protein production and purification

For SANS, CorA was produced and purified essentially as described elsewhere (*Johansen et al., 2019*). For studies in DDM, the N-terminal His-tag was cleaved by tobacco etch virus (TEV) protease before gel filtration, whereas for nanodiscs, it was cleaved after incorporation (see below). For NMR, uniformly isotopically labelled CorA was produced in M9 medium containing 3 g/L ¹³C-glucose and 1 g/L ¹⁵N-ammonium chloride. ¹⁵N-alanine-labeled CorA was produced in M9 medium containing regular ¹²C-glucose and ¹⁴N-ammonium chloride and supplemented with 200 mg/L of ¹⁵N-alanine. Match-out deuterated circularised membrane scaffold protein (MSP), d-csMSP1E3D1, was produced at the D-lab at ILL (Grenoble, France) and purified as described previously (*Johansen et al., 2019*). Proteins were stored at –80 °C until used.

CorA reconstitution in sND for SANS

CorA, d-csMSP1E3D1, and d-POPC solubilized in cholate were mixed in a ratio of 1:4:400 with a final d-POPC concentration of 10 mM. Cholate and DDM were removed by adding 50 % w/v amberlite XAD-2 overnight at 5 °C. CorA-loaded sNDs were purified by IMAC on NiNTA resin, added TEV protease and dialysed for three hours at RT followed by ON dialysis at 4 °C against 20 mM TrisHCl pH 8, 100 mM NaCl, 0.5 mM EDTA, 1 mM DTT. Finally, the cleaved sample was purified by reverse IMAC on NiNTA resin. The sample was concentrated to approximately 30 μM before the SANS experiment.

Reconstitution into multilamellar vesicles for NMR

CorA was reconstituted into DMPC at a lipid-to-protein ratio of 0.5 (w/w) by dialysis against 10 mM Tris-HCl pH 8, 40 mM MgCl₂, 1 mM methyl-β-cyclodextrin using a 25 kDa MWCO membrane at RT. A white precipitate of multilamellar vesicles was visible after 48 hr and collected by centrifugation after

72 hr. Samples were packed into 1.3 mm or 0.7 mm MAS NMR rotors using an ultracentrifuge tool (Giotto Biotech) at 100,000 g for 1 hr.

SEC-SANS

Samples were measured at the D22 beamline at ILL, using the SEC-SANS mode described elsewhere (*Johansen et al., 2018; Jordan et al., 2016*), but with the upgrade that UV absorption was measured on the flow cell in the same place, but perpendicular to the neutron beam. The setup was placed in a temperature-controlled cabinet at 11 °C. CorA in sDDM was run on a Superdex200 Increase 10/300 GL column (GE Healthcare) in 20 mM TrisDCl pH 7.5, 150 mM NaCl, 1 mM DTT, 0.5 mM sDDM in D₂O with an initial flow rate of 0.3 ml/min to allow full exchange into sDDM (*Midtgaard et al., 2018*). CorA in sND was run on a Superose6 Increase 10/300 GL column (GE Healthcare) in 20 mM TrisDCl pH 7.5, 150 mM NaCl, 1 mM DTT in D₂O with an initial flow rate of 0.5 ml/min. For all samples, the flow was reduced to 0.05 ml/min during elution of the main peak. Measurements were run twice to obtain data from two sample-to-detector distances, 2 m and 11 m, yielding data in a q -range of 0.0044 Å⁻¹ to 0.42 Å⁻¹ with the neutron wavelength of 6 Å. The scattering intensity, $I(q)$, was brought to absolute scale in units of cm⁻¹ by normalizing to the direct beam intensity measured with an attenuator in place. All SANS data and metafiles are from ILL-DATA.8-03-940 as in <https://doi.ill.fr/105291/ILL-DATA8-03-940>.

Pair distance, $p(r)$, distributions were calculated by Bayesian indirect Fourier transformation at the bayesapp server (*Hansen, 2014*) (available from the genapp server at <https://somo.chem.utk.edu/bayesapp/>). $p(r)$ s and the corresponding $I(q)$ s for PDB structures were calculated using CaPP (available at github.com/Niels-Bohr-Institute-XNS-StructBiophys/CaPP, copy archived at [swh:1:rev:210c-958f0aa476a2194871ced15513c5545da8aa](https://swh.1:rev:210c-958f0aa476a2194871ced15513c5545da8aa), *Larsen, 2022*) with a water layer excess density of 6% applied to the parts of the protein outside the membrane.

Model building

For use in both SANS comparison, normal mode analysis, and simulations, we rebuilt the missing residues and sidechains of the closed PDB structure 4I0U. The 2–6 missing residues at each chain terminus was rebuilt using Modeller's automodel functionality (*Webb and Sali, 2017*). In the open cryo-EM structures, between 18 and 20 residues were missing in the N-terminus. These were rebuilt from the closed X-ray structure (4I0U) to allow for direct comparison to SANS measurements.

Normal mode analysis

Non-linear normal mode analysis was performed using the Non-Linear rigid Block NMA (*Hoffmann and Grudinin, 2017*) (NOLB) routine (NOLB, RRID:SCR_021954). The NOLB routine was integrated with PEPSI-SANS 2.2 (PEPSI-SANS, RRID:SCR_021950) and a regularization algorithm to avoid unphysical structures. In the latter, $T = \chi^2 + \alpha S$ is minimized, where S constraints the secondary structure deviation. Scanning over different values of α , a plot of χ^2 vs. S is obtained. The best compromise between conservation of structure and the best fit to the data is chosen from the 'elbow'-region (*Figure 4—figure supplement 2*).

Metadynamics and reweighting

The simulation system was set up using the MARTINI3.0b coarse grained force field (Martini3, RRID:SCR_021951) (*Marrink, 2021*) with elastic networks terms applied to the individual chains only with a 0.9nm cut-off and a force constant of 500kJ/(mol nm²). As MARTINI does not contain parameters for protein-bound Mg²⁺ but rather models it as a free ligand with four waters bound, the Mg²⁺ ions bound in the structure were deleted. To avoid overly electrostatic repulsions from the remaining Mg²⁺ coordinating amino acids (Asp89, Asp179, Asp253 and Glu88), they were transformed into their protonated states. The POPC membrane was obtained from CHARMM-GUI (*Jo et al., 2009; Qi et al., 2015*) using 450 POPCs in each bilayer, ensuring that the entire system was big enough for larger conformational changes. The system was solvated with the MARTINI non-polarizable water and neutralized with 300mM NaCl comparable to the SANS experimental set-up. The equilibration was performed according to the CHARMM-GUI equilibration protocol using a minimization step followed by six equilibration steps with slow decrease in the positional restraint forces on both lipids and protein in each step (*Qi et al., 2015*).

The GROMACS-5.1.4 software package (GROMACS, RRID:SCR_014565) (Abraham *et al.*, 2015) was used to simulate with a 20 fs time step. Temperature and semi-isotropic pressure were controlled at 303.15K and 1bar using the stochastic velocity rescaling thermostat (Bussi *et al.*, 2007) and Parrinello-Rahman barostat (Parrinello and Rahman, 1981). Electrostatic interactions were treated using the reaction field approach. The cutoff of short-range distance for the electrostatic interactions was 1.1nm. The potential shift Verlet scheme was used to cut off the Lennard-Jones potential at long ranges.

Well-Tempered Metadynamics (Barducci *et al.*, 2008) simulations were performed with the PLUMED2.3.0 software (PLUMED 2, RRID:SCR_021952) (Tribello *et al.*, 2014). A radius of gyration collective variable was applied on all backbone beads for the intracellular residues 170-190 and 220-250 of all five chains. The metadynamics parameters were set as follows: Gaussian width = 0.05, Gaussian height = 2.1, Gaussian deposition stride = 100, biasfactor = 15 and an upper wall defined at a CV radius of gyration of 4.0nm. The wall was defined as a harmonic restraint with a force constant = 10000, harmonic exponential power = 4, off-set = 0, and a rescaling factor of 1. Multiple wall types and sizes were attempted, with lower walls causing too little dynamics for fitting with the experimental SANS data and higher walls causing individual monomers to bend unphysically and giving an unfeasible large sample space. Clustering of the simulation trajectory was performed using the KMeans clustering method (Tiberti *et al.*, 2015).

The software program BME (BME, RRID: SCR_021953) was used to reweight the MetaD trajectory to fit the experimental SANS data (Bottaro *et al.*, 2020). The hyperparameter θ was determined based on a L-curve analysis (analogous to the procedure in normal mode analysis, see **Figure 4—figure supplement 2**) of S_{rel} vs χ^2 , where θ is chosen where a natural kink is observed and any further decrease in χ^2 gives rise to an increasing larger penalty in S_{rel} . As the simulations are not fully converged and the chosen force field is coarse grained, we set the trust in the force field lower and chose a slightly lower θ -value than the kink observed.

To account for a fixed fraction of symmetric pentamers, a differential intensity was derived by $I_{diff} = I_{exp} - f \cdot I_{calc, 5sym}$, where f is the fraction of symmetric pentamer, I_{exp} is the experimental SANS data, and $I_{calc, 5sym}$ is the SANS signal of PDB 410U calculated by PEPSI-SANS. The forward scattering of the calculated SANS signal, $I_{calc, 5sym}(0)$, was scaled to match the forward scattering of the experimental SANS data. Reweighting was done against the differential SANS signal.

Solid-state NMR spectroscopy

Spectra of uniformly labelled samples were measured at a magnetic field of either 19.5T or 23.4T corresponding to a ^1H Larmor frequency of 800 MHz and 1000 MHz, respectively. The spectrometers were equipped with a Bruker 0.7 mm MAS probe, spinning at 107 kHz, at a constant temperature of 300 K. Spectra of ^{15}N Ala-labeled samples were acquired at 23.4T on a Bruker 1.3 mm MAS probe, spinning at 60 kHz, at a constant temperature of 300 K. The assignment of backbone resonances was obtained by acquiring a set of eleven ^1H -detected 3D experiments as described elsewhere (Schubeis *et al.*, 2018; Lalli *et al.*, 2017). This set notably involved six amide-detected experiments [(H)CANH, (H)CONH, (H)(CO)CA(CO)NH, (H)CO(CA)NH, (H)(CA)CB(CA)NH, (H)(CA)CB(CACO)NH] (Barbet-Massin *et al.*, 2014) and five $\text{H}\alpha$ -detected experiments [(H)NCAHA, (H)N(CO)CAHA, (H)COCAHA, (H)CO(N)CAHA, (H)CBCAHA] (Stanek *et al.*, 2016), linking resonances over neighboring residues thanks to common ^{13}C or ^{15}N shifts. Adamantane was used as the external reference. Spectral analysis and assignment were accomplished with CcpNmr Analysis (CCPN Analysis, RRID:SCR_016984) (Vranken *et al.*, 2005) and FLYA (Schmidt and Güntert, 2012) available from the CYANA program package (CYANA, RRID:SCR_014229).

Relaxation experiments were based on a ^1H , ^{15}N ^1H -detected CP-HSQC experiment incorporating an appropriate relaxation delay (Knight *et al.*, 2012). 38 and 33 residues spanning different regions of the proteins were used for the uniformly labelled sample in the presence and in the absence of Mg^{2+} , respectively. The measurements of site-specific ^{15}N $R_{1\rho}$ rates were performed at 107 kHz MAS, 19.5T and 300 K or 280 K, using relaxation delays of 0.05, 1, 5, 15, 50, 100, 200 ms under a spin-lock field of 15 kHz. Measurements of bulk ^{15}N R_1 were performed at 107 kHz MAS, 19.5T and 300 K, using relaxation delays of 0.5, 1, 2.8, 6.8, 15.8, 23.8, 53.5, 80 s. Measurements of ^{15}N $R_{1\rho}$ rates were additionally performed on the ^{15}N Ala labelled samples in the presence and in the absence of Mg^{2+} at 60 kHz MAS, 23.5T and 300 K using relaxation delays of 0.1, 1, 5, 10, 25, 50, 100ms under a spin-lock

Table 1. Negative stain EM statistics for 3D model refinement.

Parameter	1 mM EDTA	40 mM MgCl ₂
Pixel size, Å	3.14	3.14
Number of micrographs	436	440
Number of picked particles	193,606	185,577
Final number of particles	36,176	46,544
Resolution, Å	≈ 15	≈ 15

field of 15 kHz. The relaxation rates were obtained by fitting the experimental decay curves with a mono-exponential function. The error was estimated from the experimental noise by use of a Monte-Carlo evaluation.

Activity assay

Large unilamellar vesicles of POPC were prepared by dissolving a lipid film in 10 mM MOPS-KOH pH 7.2, 150 mM KCl, 100 μM EGTA including 10 μM Mag-Fluo-4 (Thermo) to a POPC concentration of 15 mg/ml, which was extruded through 0.2 μm membrane filters for 35 times using a mini-extruder (Avanti Polar Lipids). CorA was inserted by mixing a sample of 10.5 mg/ml LUVs, 2 μM CorA, 10 μM Mag-Fluo-4 and 50 mM octyl glucoside. Biobeads SM-2 were added to 45 % w/v and incubated at RT for 30 min, before purifying and at the same time exchanging the extravesicular buffer to measurement buffer (10 mM MOPS-KOH pH 7.2, 150 N-methyl-D-glucamine-HCl, 100 μM EGTA) on Sephadex G50 resin. 20 μl of CorA-LUVs (or plain LUVs) were diluted to a total of 1 ml in measurement buffer (prepared in H₂O or D₂O, respectively) containing 10 μM valinomycin with or without 1 mM Co[NH₃]³⁺ present. CorA activity was monitored by Mag-Fluo-4 fluorescence at 515 nm (excitation at 488 nm) on a FluoroMax fluorometer (Horiba) upon addition of 10 mM MgCl₂ (from a 1 M stock prepared in H₂O or D₂O, respectively). The signal was normalized to the flat signal recorded before addition of MgCl₂.

Negative stain EM

CorA was purified by SEC and diluted to 0.1 μM in appropriate buffers containing 1 mM EDTA or 40 mM Mg²⁺. Copper grids were neutralized with an Easiglow glow discharger (Agar Scientific). 3 μl of sample was applied to the grid and incubated for 30 s. The grid was blotted onto a filter paper from the edge, and 3 μL of 2% uranyl formate was added immediately and incubated for 30 s. The staining procedure was repeated two more times. After the final staining, the grid was left to dry for ten minutes. EM data were acquired on a Tecnai TEM (FEI, Thermo Fischer scientific) at Aarhus University, Denmark. The micrographs were processed by XMIPP to *.mcp files, and particle picking, 2D class averages and 3D model refinement was done in Relion 3.0. Statistics for the 3D refinement are given in **Table 1**.

Molecular graphics were performed with UCSF Chimera, developed by the Resource for Biocomputing, Visualization, and Informatics at the University of California, San Francisco, with support from NIH P41-GM103311 (Pettersen et al., 2004).

Acknowledgements

We thank Elliot Gilbert for his assistance with SANS experiments at QUOKKA at ANSTO and Marta Brennich for her assistance with SAXS experiments at BM29 at the ESRF. Thomas Boesen is acknowledged for his help with EM experiments conducted at Aarhus University and Michael Gajhede for his assistance in EM data processing. We thank Ida Louise Jørgensen for helping with functional reconstitution of CorA in large unilamellar vesicles and Michael Maguire for providing a plasmid encoding CorA.

Additional information

Funding

Funder	Grant reference number	Author
Lundbeckfonden	R155-2015-2666	Kresten Lindorff-Larsen Lise Arleth
Novo Nordisk Fonden	NNF15OC0016670	Lise Arleth
Biotechnology and Biological Sciences Research Council	BB/R00126X/1	Mark SP Sansom
Biotechnology and Biological Sciences Research Council	BB/N000145/1	Mark SP Sansom
Engineering and Physical Sciences Research Council	EP/R004722/1	Mark SP Sansom
Engineering and Physical Sciences Research Council	EP/R029407/1	Mark SP Sansom
Engineering and Physical Sciences Research Council	EP/V010948/1	Mark SP Sansom
Wellcome Trust	208361/Z/17/Z	Mark SP Sansom
National Collaborative Research Infrastructure Strategy		Tamim Darwish
European Commission	INFRAIA-01-2018-2019 GA 871037 (iNext Discovery)	Tobias Schubeis Guido Pintacuda
Villum Fonden	35955	Nicolai Tidemand Johansen
Horizon 2020 - Research and Innovation Framework Programme	ERC-2015-CoG GA 648974	Guido Pintacuda

The funders had no role in study design, data collection and interpretation, or the decision to submit the work for publication.

Author contributions

Nicolai Tidemand Johansen, Conceptualization, Formal analysis, Investigation, Project administration, Validation, Visualization, Writing – original draft, Writing – review and editing; Marta Bonaccorsi, Formal analysis, Investigation, Methodology, Validation, Visualization, Writing – original draft, Writing – review and editing; Tone Bengtsen, Data curation, Formal analysis, Methodology, Software, Visualization, Writing – review and editing; Andreas Haahr Larsen, Data curation, Formal analysis, Investigation, Resources, Software, Visualization, Writing – review and editing; Frederik Grøn­bæk Tidemand, Pie Huda, Investigation, Resources, Writing – review and editing; Martin Cramer Pedersen, Formal analysis, Investigation, Supervision, Visualization, Writing – original draft; Jens Berndtsson, Resources, Writing – review and editing; Tamim Darwish, Funding acquisition, Project administration, Writing – review and editing; Nageshewar Rao Yepuri, Resources, Visualization, Writing – review and editing; Anne Martel, Data curation, Resources, Writing – review and editing; Thomas Günther Pomorski, Mikaela Rapp, Supervision, Writing – review and editing; Andrea Bertarello, Formal analysis, Investigation, Writing – review and editing; Mark Sansom, Funding acquisition, Supervision, Writing – review and editing; Ramon Crehuet, Methodology, Software, Writing – review and editing; Tobias Schubeis, Conceptualization, Formal analysis, Investigation, Supervision, Visualization, Writing – original draft, Writing – review and editing; Kresten Lindorff-Larsen, Guido Pintacuda, Lise Arleth, Conceptualization, Funding acquisition, Supervision, Writing – original draft, Writing – review and editing, Investigation

Author ORCIDs

Nicolai Tidemand Johansen  <http://orcid.org/0000-0002-8596-548X>

Marta Bonaccorsi [ib](http://orcid.org/0000-0001-6177-0701) <http://orcid.org/0000-0001-6177-0701>
 Tone Bengtsen [ib](http://orcid.org/0000-0001-8423-2156) <http://orcid.org/0000-0001-8423-2156>
 Andreas Haahr Larsen [ib](http://orcid.org/0000-0002-2230-2654) <http://orcid.org/0000-0002-2230-2654>
 Frederik Grønbaek Tidemand [ib](http://orcid.org/0000-0001-8914-9626) <http://orcid.org/0000-0001-8914-9626>
 Martin Cramer Pedersen [ib](http://orcid.org/0000-0002-8982-7615) <http://orcid.org/0000-0002-8982-7615>
 Pie Huda [ib](http://orcid.org/0000-0002-2197-4993) <http://orcid.org/0000-0002-2197-4993>
 Jens Berndtsson [ib](http://orcid.org/0000-0001-6627-8134) <http://orcid.org/0000-0001-6627-8134>
 Tamim Darwish [ib](http://orcid.org/0000-0001-7704-1837) <http://orcid.org/0000-0001-7704-1837>
 Nageshwar Rao Yepuri [ib](http://orcid.org/0000-0002-4665-1306) <http://orcid.org/0000-0002-4665-1306>
 Thomas Günther Pomorski [ib](http://orcid.org/0000-0002-4889-0829) <http://orcid.org/0000-0002-4889-0829>
 Andrea Bertarello [ib](http://orcid.org/0000-0003-3705-1760) <http://orcid.org/0000-0003-3705-1760>
 Mark Sansom [ib](http://orcid.org/0000-0001-6360-7959) <http://orcid.org/0000-0001-6360-7959>
 Mikaela Rapp [ib](http://orcid.org/0000-0002-4401-9518) <http://orcid.org/0000-0002-4401-9518>
 Ramon Crehuet [ib](http://orcid.org/0000-0002-6687-382X) <http://orcid.org/0000-0002-6687-382X>
 Tobias Schubeis [ib](http://orcid.org/0000-0003-2203-1126) <http://orcid.org/0000-0003-2203-1126>
 Kresten Lindorff-Larsen [ib](http://orcid.org/0000-0002-4750-6039) <http://orcid.org/0000-0002-4750-6039>
 Guido Pintacuda [ib](http://orcid.org/0000-0001-7757-2144) <http://orcid.org/0000-0001-7757-2144>
 Lise Arleth [ib](http://orcid.org/0000-0002-4694-4299) <http://orcid.org/0000-0002-4694-4299>

Decision letter and Author response

Decision letter <https://doi.org/10.7554/eLife.71887.sa1>

Author response <https://doi.org/10.7554/eLife.71887.sa2>

Additional files

Supplementary files

- Transparent reporting form

Data availability

SANS data have been deposited in SASBDB under IDs SASDM42, SASDM52, SASDM62, SASDM72. EM data have been uploaded to the Electron Microscopy Data Bank under IDs EMD-13326 and EMD-13327. Activity (fluorescence) data have been uploaded to GitHub at <https://github.com/Niels-Bohr-Institute-XNS-StructBiophys/CorAData> (copy archived at [swh:1:rev:94c6ed6e-fa9166781a36307eb7c6d05e125ffa2d](https://www.swh.io/rev/94c6ed6e-fa9166781a36307eb7c6d05e125ffa2d)). The Metadynamics simulations have been uploaded to GitHub at <https://github.com/KULL-Centre/papers/tree/main/2021/CorA-Johansen-et-al> ([swh:1:rev:511f01bdf1c2b57d68654deee7f15ce019f65d7a](https://www.swh.io/rev/511f01bdf1c2b57d68654deee7f15ce019f65d7a)). NMR data have been deposited in Biological Magnetic Resonance Data Bank under ID 50959.

The following datasets were generated:

Author(s)	Year	Dataset title	Dataset URL	Database and Identifier
Johansen NT, Pedersen MC, Tidemand Arleth L	2021	Cobalt/magnesium transport protein CorA in matched-out deuterated dodecylmaltoside (dDDM) micelles without Mg ²⁺	https://www.sasbdb.org/data/SASDM42	SASBDB, SASDM42
Johansen NT, Pedersen MC, Tidemand Arleth L	2021	Cobalt/magnesium transport protein CorA in matched-out deuterated dodecylmaltoside (dDDM) micelles with bound Mg ²⁺	https://www.sasbdb.org/data/SASDM52	SASBDB, SASDM52
Johansen NT, Pedersen MC, Tidemand Arleth L	2021	Cobalt/magnesium transport protein CorA in matched-out deuterated nanodiscs without Mg ²⁺	https://www.sasbdb.org/data/SASDM762	SASBDB, SASDM62

Continued on next page

Continued

Author(s)	Year	Dataset title	Dataset URL	Database and Identifier
Johansen NT, Pedersen MC, Tidemand Arleth L	2021	Cobalt/magnesium transport protein CorA in match-out deuterated nanodiscs with bound Mg ²⁺	https://www.sasbdb.org/data/SASDM72	SASBDB, SASDM72
Schubeis T, Bonaccorsi M, Pintacuda G	2021	Resonance assignment of Mg-bound CorA in DMPC	https://bmrbl.io/data_library/summary/?bmrblid=50959	BMRB, ID50959
Larsen AH, Johansen NT, Arleth L	2021	T. maritima CorA in DDM micelles without Mg ²⁺ bound in D ₂ O	https://www.ebi.ac.uk/emdb/entry/EMD-13326	EMDB, EMD-13326
Larsen AH, Johansen NT, Arleth L	2021	T. maritima CorA in DDM micelles with Mg ²⁺ bound in D ₂ O	https://www.ebi.ac.uk/emdb/entry/EMD-13327	EMDB, EMD-13327

References

- Abraham MJ**, Murtola T, Schulz R, Páll S, Smith JC, Hess B, Lindahl E. 2015. GROMACS: High performance molecular simulations through multi-level parallelism from laptops to supercomputers. *SoftwareX* 1–2:19–25. DOI: <https://doi.org/10.1016/j.softx.2015.06.001>
- Barbet-Massin E**, Pell AJ, Retel JS, Andreas LB, Jaudzems K, Franks WT, Nieuwkoop AJ, Hiller M, Higman V, Guery P, Bertarello A, Knight MJ, Felletti M, Le Marchand T, Kotlovica S, Akopjana I, Tars K, Stoppini M, Bellotti V, Bolognesi M, et al. 2014. Rapid Proton-Detected NMR Assignment for Proteins with Fast Magic Angle Spinning. *Journal of the American Chemical Society* 136:12489–12497. DOI: <https://doi.org/10.1021/ja507382j>, PMID: 25102442
- Barducci A**, Bussi G, Parrinello M. 2008. Well-tempered metadynamics: a smoothly converging and tunable free-energy method. *Physical Review Letters* 100:020603. DOI: <https://doi.org/10.1103/PhysRevLett.100.020603>, PMID: 18232845
- Bonaccorsi M**, Le Marchand T, Pintacuda G. 2021. Protein structural dynamics by Magic-Angle Spinning NMR. *Current Opinion in Structural Biology* 70:34–43. DOI: <https://doi.org/10.1016/j.sbi.2021.02.008>, PMID: 33915352
- Bottaro S**, Bengtsen T, Lindorff-Larsen K. 2020. Integrating Molecular Simulation and Experimental Data: A Bayesian/Maximum Entropy Reweighting Approach. *Methods in Molecular Biology (Clifton, N.J.)* 2112:219–240. DOI: https://doi.org/10.1007/978-1-0716-0270-6_15, PMID: 32006288
- Bussi G**, Donadio D, Parrinello M. 2007. Canonical sampling through velocity rescaling. *The Journal of Chemical Physics* 126:014101. DOI: <https://doi.org/10.1063/1.2408420>, PMID: 17212484
- Chakrabarti N**, Neale C, Payandeh J, Pai EF, Pomès R. 2010. An Iris-Like Mechanism of Pore Dilation in the CorA Magnesium Transport System. *Biophysical Journal* 98:784–792. DOI: <https://doi.org/10.1016/j.bpj.2009.11.009>, PMID: 20197031
- Dalmas O**, Sandtner W, Medovoy D, Frezza L, Bezanilla F, Perozo E. 2014a. A repulsion mechanism explains magnesium permeation and selectivity in CorA. *PNAS* 111:3002–3007. DOI: <https://doi.org/10.1073/pnas.1319054111>, PMID: 24516146
- Dalmas O**, Sompornpisut P, Bezanilla F, Perozo E. 2014b. Molecular mechanism of Mg²⁺-dependent gating in CorA. *Nature Communications* 5:3590. DOI: <https://doi.org/10.1038/ncomms4590>, PMID: 24694723
- de Baaij JHF**, Hoenderop JGJ, Bindels RJM. 2015. Magnesium in man: implications for health and disease. *Physiological Reviews* 95:1–46. DOI: <https://doi.org/10.1152/physrev.00012.2014>, PMID: 25540137
- DiNicolantonio JJ**, Liu J, O’Keefe JH. 2018. Magnesium for the prevention and treatment of cardiovascular disease. *Open Heart* 5:e000775. DOI: <https://doi.org/10.1136/openhrt-2018-000775>, PMID: 30018772
- Eshaghi S**, Niegowski D, Kohl A, Martinez Molina D, Lesley SA, Nordlund P. 2006. Crystal structure of a divalent metal ion transporter CorA at 2.9 angstrom resolution. *Science (New York, N.Y.)* 313:354–357. DOI: <https://doi.org/10.1126/science.1127121>, PMID: 16857941
- Franke D**, Svergun DI. 2009. DAMMIF, a program for rapid ab-initio shape determination in small-angle scattering. *Journal of Applied Crystallography* 42:342–346. DOI: <https://doi.org/10.1107/S0021889809000338>, PMID: 27630371
- Franke D**, Petoukhov MV, Konarev PV, Panjkovich A, Tuukkanen A, Mertens HDT, Kikhney AG, Hajizadeh NR, Franklin JM, Jeffries CM, Svergun DI. 2017. ATSAS 2.8: a comprehensive data analysis suite for small-angle scattering from macromolecular solutions. *Journal of Applied Crystallography* 50:1212–1225. DOI: <https://doi.org/10.1107/S1600576717007786>, PMID: 28808438
- Guskov A**, Nordin N, Reynaud A, Engman H, Lundbäck AK, Jong AJO, Cornvik T, Phua T, Eshaghi S. 2012. Structural insights into the mechanisms of Mg²⁺ uptake, transport, and gating by CorA. *PNAS* 109:18459–18464. DOI: <https://doi.org/10.1073/pnas.1210076109>, PMID: 23091000

- Hansen S.** 2014. Update for BayesApp: a web site for analysis of small-angle scattering data. *Journal of Applied Crystallography* **47**:1469–1471. DOI: <https://doi.org/10.1107/S1600576714013156>
- Hoffmann A**, Grudin SN. 2017. NOLB: Nonlinear Rigid Block Normal-Mode Analysis Method. *Journal of Chemical Theory and Computation* **13**:2123–2134. DOI: <https://doi.org/10.1021/acs.jctc.7b00197>, PMID: 28379696
- Hummer G**, Garde S, García AE, Pratt LR. 2000. New perspectives on hydrophobic effects. *Chemical Physics* **258**:349–370. DOI: [https://doi.org/10.1016/S0301-0104\(00\)00115-4](https://doi.org/10.1016/S0301-0104(00)00115-4)
- Jahnen-Dechent W**, Ketteler M. 2012. Magnesium basics. *Clinical Kidney Journal* **5**:i3–i14. DOI: <https://doi.org/10.1093/ndtplus/sfr163>, PMID: 26069819
- Jo S**, Lim JB, Klauda JB, Im W. 2009. CHARMM-GUI Membrane Builder for mixed bilayers and its application to yeast membranes. *Biophysical Journal* **97**:50–58. DOI: <https://doi.org/10.1016/j.bpj.2009.04.013>, PMID: 19580743
- Johansen NT**, Pedersen MC, Porcar L, Martel A, Arleth L. 2018. Introducing SEC-SANS for studies of complex self-organized biological systems. *Acta Crystallographica. Section D, Structural Biology* **74**:1178–1191. DOI: <https://doi.org/10.1107/S2059798318007180>, PMID: 30605132
- Johansen NT**, Tidemand FG, Nguyen TTTN, Rand KD, Pedersen MC, Arleth L. 2019. Circularized and solubility-enhanced MSPs facilitate simple and high-yield production of stable nanodiscs for studies of membrane proteins in solution. *The FEBS Journal* **286**:1734–1751. DOI: <https://doi.org/10.1111/febs.14766>, PMID: 30675761
- Jordan A**, Jacques M, Merrick C, Devos J, Forsyth VT, Porcar L, Martel A. 2016. SEC-SANS: size exclusion chromatography combined in situ with small-angle neutron scattering. *Journal of Applied Crystallography* **49**:2015–2020. DOI: <https://doi.org/10.1107/S1600576716016514>, PMID: 27980509
- Knight MJ**, Pell AJ, Bertini I, Felli IC, Gonnelli L, Pierattelli R, Herrmann T, Emsley L, Pintacuda G. 2012. Structure and backbone dynamics of a microcrystalline metalloprotein by solid-state NMR. *PNAS* **109**:11095–11100. DOI: <https://doi.org/10.1073/pnas.1204515109>, PMID: 22723345
- Knoop V**, Groth-Maloney M, Gebert M, Eifler K, Weyand K. 2005. Transport of magnesium and other divalent cations: evolution of the 2-TM-GxN proteins in the MIT superfamily. *Molecular Genetics and Genomics* **274**:205–216. DOI: <https://doi.org/10.1007/s00438-005-0011-x>, PMID: 16179994
- Kowitz T**, Maguire ME. 2019. Loss of cytosolic Mg²⁺ binding sites in the *Thermotoga maritima* CorA Mg²⁺ channel is not sufficient for channel opening. *Biochimica et Biophysica Acta (BBA) - General Subjects* **1863**:25–30. DOI: <https://doi.org/10.1016/j.bbagen.2018.09.001>
- Lalli D**, Idso MN, Andreas LB, Hussain S, Baxter N, Han S, Chmelka BF, Pintacuda G. 2017. Proton-Based Structural Analysis of a Heptahelical Transmembrane Protein in Lipid Bilayers. *Journal of the American Chemical Society* **139**:13006–13012. DOI: <https://doi.org/10.1021/jacs.7b05269>, PMID: 28724288
- Larsen AH.** 2022. caPP 3.12. swb:1:rev:210c958f0aa476a2194871ced15513c5545da8aa. Software Heritage. <https://archive.softwareheritage.org/swb:1:dir:8145e77abb9c5b01f9f4f1cb3902d2035b588dce;origin=https://github.com/Niels-Bohr-Institute-XNS-StructBiophys/caPP;visit=swb:1:snp:4cb91dd4e4291e73b952327ba4a87e3b646832b9;anchor=swb:1:rev:210c958f0aa476a2194871ced15513c5545da8aa>
- Lunin VV**, Dobrovetsky E, Khutoreskaya G, Zhang R, Joachimiak A, Doyle DA, Bochkarev A, Maguire ME, Edwards AM, Koth CM. 2006. Crystal structure of the CorA Mg²⁺ transporter. *Nature* **440**:833–837. DOI: <https://doi.org/10.1038/nature04642>, PMID: 16598263
- Maguire ME**, Cowan JA. 2002. Magnesium chemistry and biochemistry. *Biometals: An International Journal on the Role of Metal Ions in Biology, Biochemistry, and Medicine* **15**:203–210. DOI: <https://doi.org/10.1023/a:1016058229972>, PMID: 12206387
- Maguire ME.** 2006. Magnesium transporters: properties, regulation and structure. *Frontiers in Bioscience* **11**:3149–3163. DOI: <https://doi.org/10.2741/2039>, PMID: 16720382
- Maric S**, Skar-Gislinge N, Midtgaard S, Thygesen MB, Schiller J, Frielinghaus H, Moulin M, Haertlein M, Forsyth VT, Pomorski TG, Arleth L. 2014. Stealth carriers for low-resolution structure determination of membrane proteins in solution. *Acta Crystallographica. Section D, Biological Crystallography* **70**:317–328. DOI: <https://doi.org/10.1107/S1399004713027466>, PMID: 24531466
- Marrink SJ.** 2021. Martini 3 open-beta release. Martini. <http://cgmartini.nl/index.php/martini3beta>
- Matthies D**, Dalmás O, Borgnia MJ, Dominik PK, Merk A, Rao P, Reddy BG, Islam S, Bartesaghi A, Perozo E, Subramaniam S. 2016. Cryo-EM Structures of the Magnesium Channel CorA Reveal Symmetry Break upon Gating. *Cell* **164**:747–756. DOI: <https://doi.org/10.1016/j.cell.2015.12.055>, PMID: 26871634
- Midtgaard SR**, Darwish TA, Pedersen MC, Huda P, Larsen AH, Jensen GV, Kynde SAR, Skar-Gislinge N, Nielsen AJZ, Olesen C, Blaise M, Dorosz JJ, Thorsen TS, Venskutonytė R, Krintel C, Møller JV, Frielinghaus H, Gilbert EP, Martel A, Kastrup JS, et al. 2018. Invisible detergents for structure determination of membrane proteins by small-angle neutron scattering. *The FEBS Journal* **285**:357–371. DOI: <https://doi.org/10.1111/febs.14345>, PMID: 29178440
- Neale C**, Chakrabarti N, Pomorski P, Pai EF, Pomès R. 2015. Hydrophobic Gating of Ion Permeation in Magnesium Channel CorA. *PLoS Computational Biology* **11**:e1004303. DOI: <https://doi.org/10.1371/journal.pcbi.1004303>, PMID: 26181442
- Nemchinova M**, Melcr J, Wassenaar TA, Marrink SJ, Guskov A. 2021. Asymmetric CorA Gating Mechanism as Observed by Molecular Dynamics Simulations. *Journal of Chemical Information and Modeling* **61**:2407–2417. DOI: <https://doi.org/10.1021/acs.jcim.1c00261>, PMID: 33886304

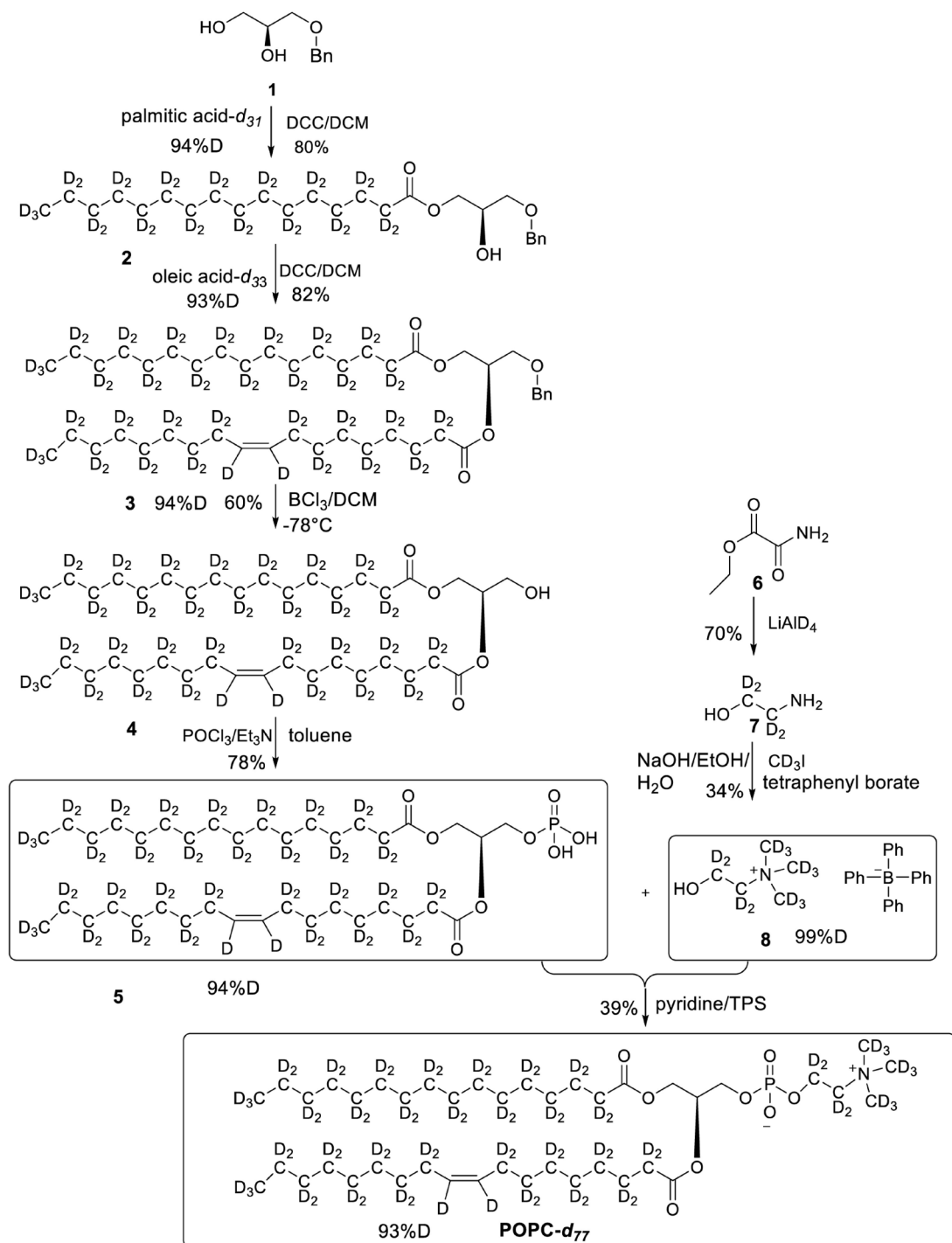
- Némethy G**, Scheraga HA. 1964. Structure of Water and Hydrophobic Bonding in Proteins. IV. The Thermodynamic Properties of Liquid Deuterium Oxide. *The Journal of Chemical Physics* **41**:680–689. DOI: <https://doi.org/10.1063/1.1725946>
- Nordin N**, Guskov A, Phua T, Sahaf N, Xia Y, Lu S, Eshaghi H, Eshaghi S. 2013. Exploring the structure and function of *Thermotoga maritima* CorA reveals the mechanism of gating and ion selectivity in Co²⁺/Mg²⁺ transport. *The Biochemical Journal* **451**:365–374. DOI: <https://doi.org/10.1042/BJ20121745>, PMID: 23425532
- Palombo I**, Daley DO, Rapp M. 2013. Why is the GMN motif conserved in the CorA/Mrs2/Alr1 superfamily of magnesium transport proteins? *Biochemistry* **52**:4842–4847. DOI: <https://doi.org/10.1021/bi4007397>, PMID: 23781956
- Papp-Wallace KM**, Maguire ME. 2007. Bacterial homologs of eukaryotic membrane proteins: the 2-TM-GxN family of Mg(2+) transporters. *Molecular Membrane Biology* **24**:351–356. DOI: <https://doi.org/10.1080/09687680701441883>, PMID: 17710639
- Parrinello M**, Rahman A. 1981. Polymorphic transitions in single crystals: A new molecular dynamics method. *Journal of Applied Physics* **52**:7182–7190. DOI: <https://doi.org/10.1063/1.328693>
- Payandeh J**, Pai EF. 2006. A structural basis for Mg²⁺ homeostasis and the CorA translocation cycle. *The EMBO Journal* **25**:3762–3773. DOI: <https://doi.org/10.1038/sj.emboj.7601269>, PMID: 16902408
- Payandeh J**, Li C, Ramjeesingh M, Poduch E, Bear CE, Pai EF. 2008. Probing structure-function relationships and gating mechanisms in the CorA Mg²⁺ transport system. *The Journal of Biological Chemistry* **283**:11721–11733. DOI: <https://doi.org/10.1074/jbc.M707889200>, PMID: 18276588
- Pedersen MC**, Arleth L, Mortensen K. 2013. WillItFit: a framework for fitting of constrained models to small-angle scattering data. *Journal of Applied Crystallography* **46**:1894–1898. DOI: <https://doi.org/10.1107/S0021889813026022>
- Pettersen EF**, Goddard TD, Huang CC, Couch GS, Greenblatt DM, Meng EC, Ferrin TE. 2004. UCSF Chimera—a visualization system for exploratory research and analysis. *Journal of Computational Chemistry* **25**:1605–1612. DOI: <https://doi.org/10.1002/jcc.20084>, PMID: 15264254
- Pfoh R**, Li A, Chakrabarti N, Payandeh J, Pomès R, Pai EF. 2012. Structural asymmetry in the magnesium channel CorA points to sequential allosteric regulation. *PNAS* **109**:18809–18814. DOI: <https://doi.org/10.1073/pnas.1209018109>, PMID: 23112165
- Qi Y**, Ingólfsson HI, Cheng X, Lee J, Marrink SJ, Im W. 2015. CHARMM-GUI Martini Maker for Coarse-Grained Simulations with the Martini Force Field. *Journal of Chemical Theory and Computation* **11**:4486–4494. DOI: <https://doi.org/10.1021/acs.jctc.5b00513>, PMID: 26575938
- Rangl M**, Schmandt N, Perozo E, Scheuring S. 2019. Real time dynamics of Gating-Related conformational changes in CorA. *eLife* **8**:e47322. DOI: <https://doi.org/10.7554/eLife.47322>, PMID: 31774394
- Rao S**, Klesse G, Lynch CI, Tucker SJ, Sansom MSP. 2021. Molecular Simulations of Hydrophobic Gating of Pentameric Ligand Gated Ion Channels: Insights into Water and Ions. *The Journal of Physical Chemistry B* **125**:981–994. DOI: <https://doi.org/10.1021/acs.jpcc.0c09285>, PMID: 33439645
- Reif B**, Ashbrook SE, Emsley L, Hong M. 2021. Solid-state NMR spectroscopy. *Nature Reviews. Methods Primers* **1**:2. DOI: <https://doi.org/10.1038/s43586-020-00002-1>, PMID: 34368784
- Rude RK**. 1998. Magnesium deficiency: a cause of heterogeneous disease in humans. *Journal of Bone and Mineral Research* **13**:749–758. DOI: <https://doi.org/10.1359/jbmr.1998.13.4.749>, PMID: 9556074
- Schmidt E**, Güntert P. 2012. A New Algorithm for Reliable and General NMR Resonance Assignment. *Journal of the American Chemical Society* **134**:12817–12829. DOI: <https://doi.org/10.1021/ja305091n>, PMID: 22794163
- Schubeis T**, Le Marchand T, Andreas LB, Pintacuda G. 2018. 1H magic-angle spinning NMR evolves as a powerful new tool for membrane proteins. *Journal of Magnetic Resonance (San Diego, Calif)* **287**:140–152. DOI: <https://doi.org/10.1016/j.jmr.2017.11.014>, PMID: 29413327
- Schubeis T**, Le Marchand T, Daday C, Kopec W, Tekwani Movellan K, Stanek J, Schwarzer TS, Castiglione K, de Groot BL, Pintacuda G, Andreas LB. 2020. A β -barrel for oil transport through lipid membranes: Dynamic NMR structures of AlkL. *PNAS* **117**:21014–21021. DOI: <https://doi.org/10.1073/pnas.2002598117>, PMID: 32817429
- Skar-Gislinge N**, Simonsen JB, Mortensen K, Feidenhans'l R, Sligar SG, Lindberg Møller B, Bjørnholm T, Arleth L. 2010. Elliptical structure of phospholipid bilayer nanodiscs encapsulated by scaffold proteins: casting the roles of the lipids and the protein. *Journal of the American Chemical Society* **132**:13713–13722. DOI: <https://doi.org/10.1021/ja1030613>, PMID: 20828154
- Smart OS**, Neduvellil JG, Wang X, Wallace BA, Sansom MSP. 1996. HOLE: a program for the analysis of the pore dimensions of ion channel structural models. *Journal of Molecular Graphics* **14**:354–360. DOI: [https://doi.org/10.1016/s0263-7855\(97\)00009-x](https://doi.org/10.1016/s0263-7855(97)00009-x), PMID: 9195488
- Stanek J**, Andreas LB, Jaudzems K, Cala D, Lalli D, Bertarello A, Schubeis T, Akopjana I, Kotelovica S, Tars K, Pica A, Leone S, Picone D, Xu ZQ, Dixon NE, Martinez D, Berbon M, El Mammeri N, Noubhani A, Saupe S, et al. 2016. NMR Spectroscopic Assignment of Backbone and Side-Chain Protons in Fully Protonated Proteins: Microcrystals, Sedimented Assemblies, and Amyloid Fibrils. *Angewandte Chemie International Edition* **55**:15504–15509. DOI: <https://doi.org/10.1002/anie.201607084>, PMID: 27865050
- Sugiyama T**, Yoshiok T. 2012. Functional Difference Between Deuterated and Protonated Macromolecules. *InTech*. DOI: <https://doi.org/10.5772/36649>
- Tiberti M**, Papaleo E, Bengtsen T, Boomsma W, Lindorff-Larsen K. 2015. ENCORE: Software for Quantitative Ensemble Comparison. *PLOS Computational Biology* **11**:1004415. DOI: <https://doi.org/10.1371/journal.pcbi.1004415>, PMID: 26505632

- Tribello GA**, Bonomi M, Branduardi D, Camilloni C, Bussi G. 2014. PLUMED 2: New feathers for an old bird. *Computer Physics Communications* **185**:604–613. DOI: <https://doi.org/10.1016/j.cpc.2013.09.018>
- Vranken WF**, Boucher W, Stevens TJ, Fogh RH, Pajon A, Llinas M, Ulrich EL, Markley JL, Ionides J, Laue ED. 2005. The CCPN data model for NMR spectroscopy: Development of a software pipeline. *Proteins* **59**:687–696. DOI: <https://doi.org/10.1002/prot.20449>, PMID: 15815974
- Webb B**, Sali A. 2017. Protein Structure Modeling with MODELLER. *Methods in Molecular Biology (Clifton, N.J.)* **1654**:39–54. DOI: https://doi.org/10.1007/978-1-4939-7231-9_4, PMID: 28986782
- Yepuri NR**, Darwish TA, Krause-Heuer AM, Leung AE, Delhom R, Wacklin HP, Holden PJ. 2016. Synthesis of Perdeuterated 1-Palmitoyl-2-oleoyl- sn -glycero-3-phosphocholine ([D 82]POPC) and Characterisation of Its Lipid Bilayer Membrane Structure by Neutron Reflectometry. *ChemPlusChem* **81**:315–321. DOI: <https://doi.org/10.1002/cplu.201500452>
- Zhang Y**, Dijkman PM, Zou R, Zandl-Lang M, Sanchez RM, Eckhardt-Strelau L, Köfeler H, Vogel H, Yuan S, Kudryashev M. 2021. Asymmetric opening of the homopentameric 5-HT3A serotonin receptor in lipid bilayers. *Nature Communications* **12**:1074. DOI: <https://doi.org/10.1038/s41467-021-21016-7>, PMID: 33594077

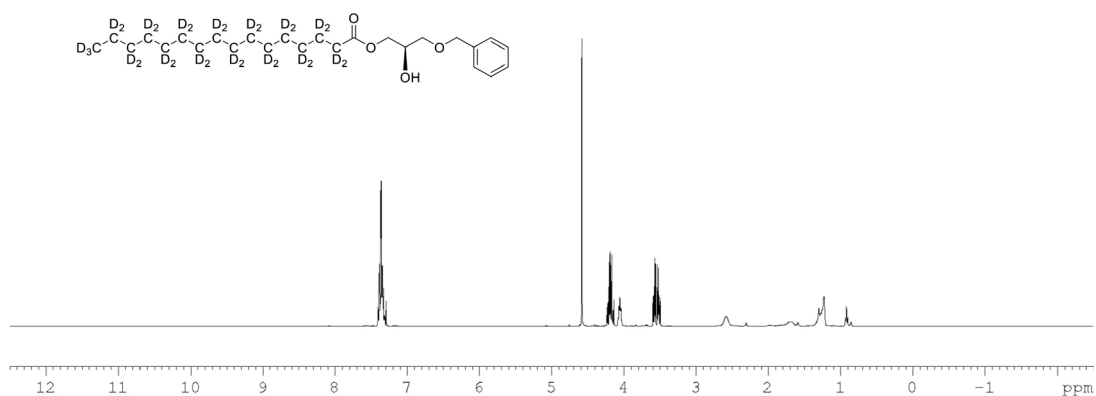
Appendix 1

Synthesis of match-out deuterated POPC

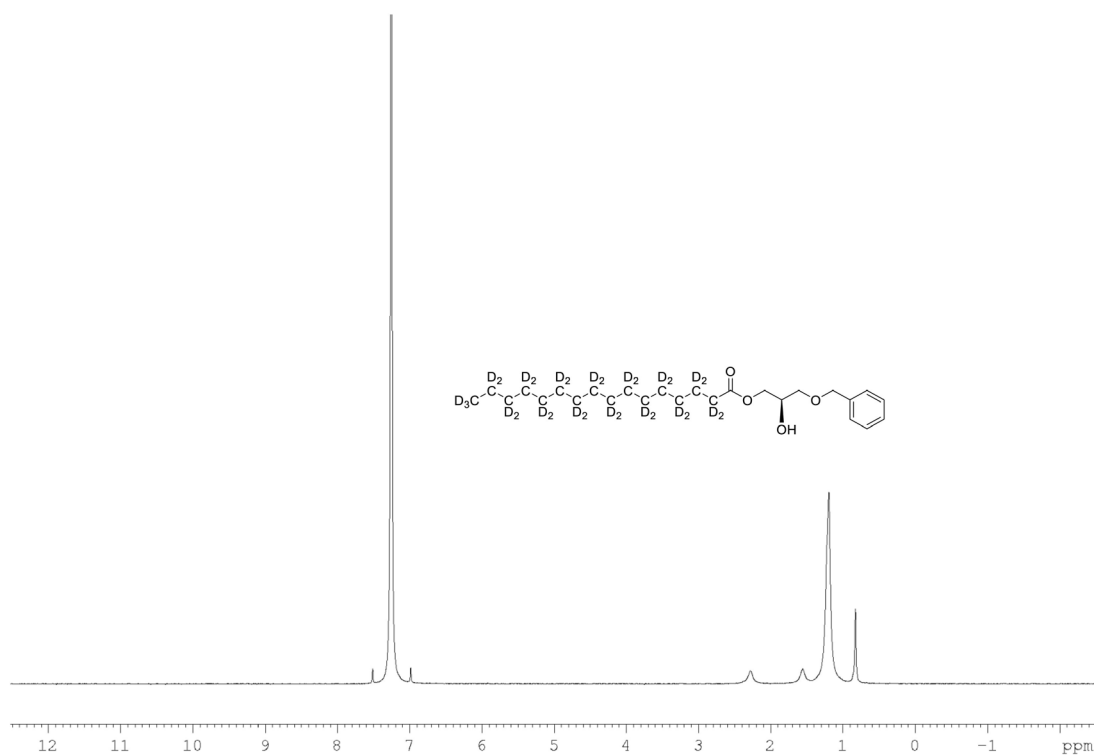
The overall synthesis of POPC- d_{77} is reported elsewhere (Yepuri *et al.*, 2016). **Appendix 1—figure 1** shows the synthetic scheme followed in this study to produce the specific level of deuteration in the head and tail groups of the POPC. The specific level of deuteration in the tail group was achieved by diluting pure heavy water with light water in specific ratios in the Parr reactor when making the deuterated alkyl chains from their fatty acid precursors (Midtgaard *et al.*, 2018). The analysis data and spectra of the intermediate compounds and the final compound are shown in **Appendix 1—figures 2–24**. Electrospray ionisation mass spectra (ESI-MS) were recorded on a 4,000 QTrap AB SCIEX Mass Spectrometer. The overall percent deuteration of the molecules was calculated by ER-MS (enhanced resolution – MS) using the isotope distribution analysis of the different isotopologues by analysing the area under each MS peak which corresponds to a defined number of deuterium atoms. The contribution of the carbon-13 (natural abundance) to the value of the area under each $[X + 1]$ MS signal is subtracted based on the relative amount found in the protonated version. In a typical analysis we measure the C-13 natural abundance contribution by running ER-MS of the protonated version (or estimate it by ChemDraw software) and use this value in our calculation using an in-house developed method that subtracts this contribution from each MS signal constituting the isotope distribution. ^1H NMR (400 MHz), ^{13}C NMR (100 MHz), ^{31}P NMR (162 MHz) and ^2H NMR (61.4 MHz) spectra were recorded on a Bruker 400 MHz spectrometer at 298 K. Chemical shifts, in ppm, were referenced to the residual signal of the corresponding solvent. Deuterium NMR spectroscopy was performed using the probe's lock channel for direct observation.



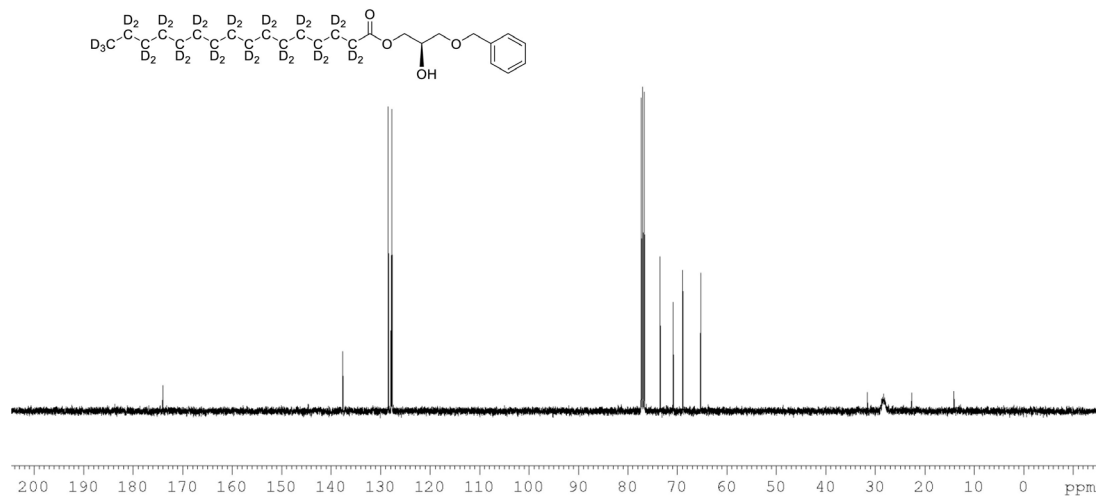
Appendix 1—figure 1. Overall synthesis achieved by following a reported paper, all the intermediates and final POPC- d_{77} were obtained in similar yields (Yepuri *et al.*, 2016).



Appendix 1—figure 2. ^1H NMR of 1-palmitoyl- d_{31} -sn-3-benzyloxy-glycerol (**Appendix 1—figure 1**, molecule 2) in CDCl_3 . (400 MHz, CDCl_3), δ residual protons 0.88 (m, 0.22 H), 1.10–1.7 (m, 1.96 H), 1.57.1.86 (m, 1.55 H), 1.96 (m, 0.54 H), 3.69 (m, 2 H), 4.09 (m, 1 H), 4.22 (m, 2 H) 4.60 (s, 2 H), 7.36 (m, 5 H).



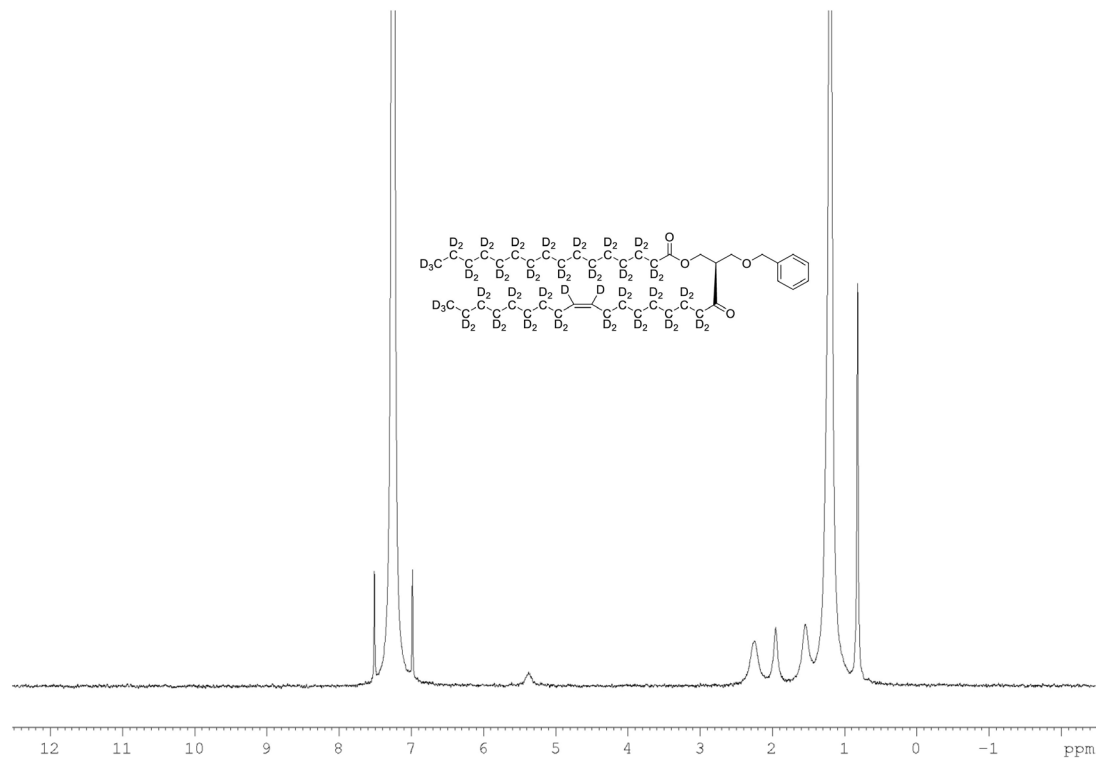
Appendix 1—figure 3. ^2H NMR of 1-palmitoyl- d_{31} -sn-3-benzyloxy-glycerol (**Appendix 1—figure 1**, molecule 2) in CDCl_3 . (400 MHz, CDCl_3), δ 0.82 (m), 1.18 (m), 1.54 (m), 2.27 (m).



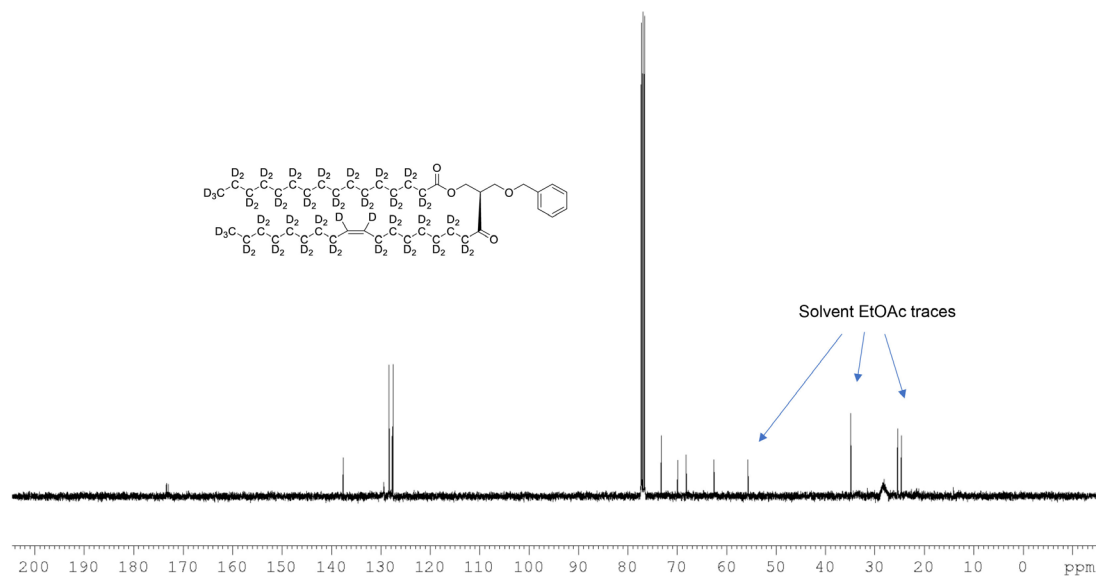
Appendix 1—figure 4. ^{13}C NMR of 1-palmitoyl- d_{31} -sn-3-benzyloxy-glycerol (**Appendix 1—figure 1**, molecule 2) in CDCl_3 . (400 MHz, CDCl_3), 10.9 (m), 22.09 (m), 28.33 (m), 33.05 (m), 65.33, 68.9, 70.80, 73.5, 127.7, 127.9, 128.5, 137.6, 174.0.



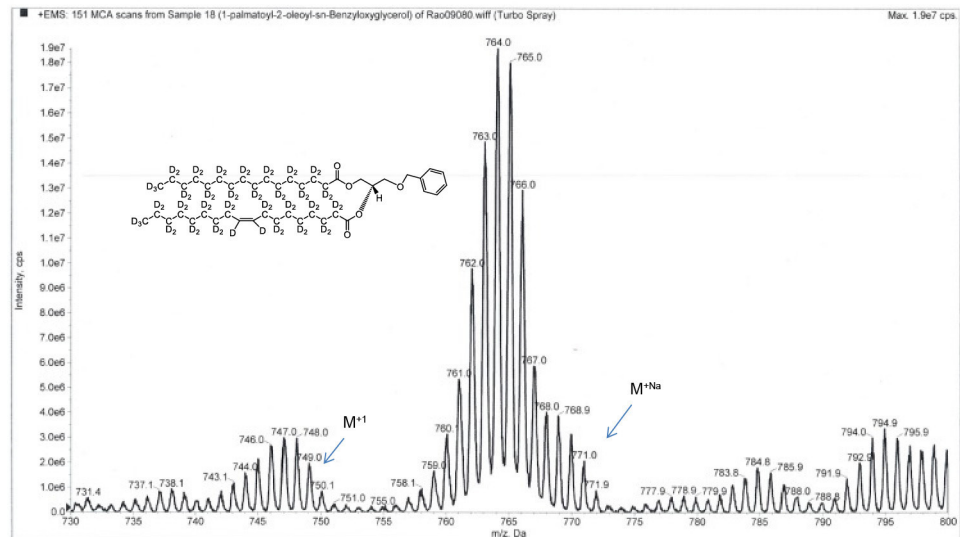
Appendix 1—figure 5. ^1H NMR of 1-palmitoyl- d_{31} -2-oleoyl- d_{33} -sn-3-benzyloxy-glycerol (**Appendix 1—figure 1**, molecule 3) in CDCl_3 . (400 MHz, CDCl_3), δ residual protons 0.90 (m, 3.56 H), 1.29 (m, 5.15 H), 1.98 (m, 0.68 H), 2.29 (m, 1.25 H), 3.61 (d, $J = 5.0$ Hz, 2 H), 4.21 (m, 1 H), 4.36 (m, 1 H), protonated benzyl protons 4.56 (AB q, $J = 12$ Hz, 2 H), 5.26 (m, 1 H), 5.35 (s, 0.65 H), 7.34 (m, 5 H).



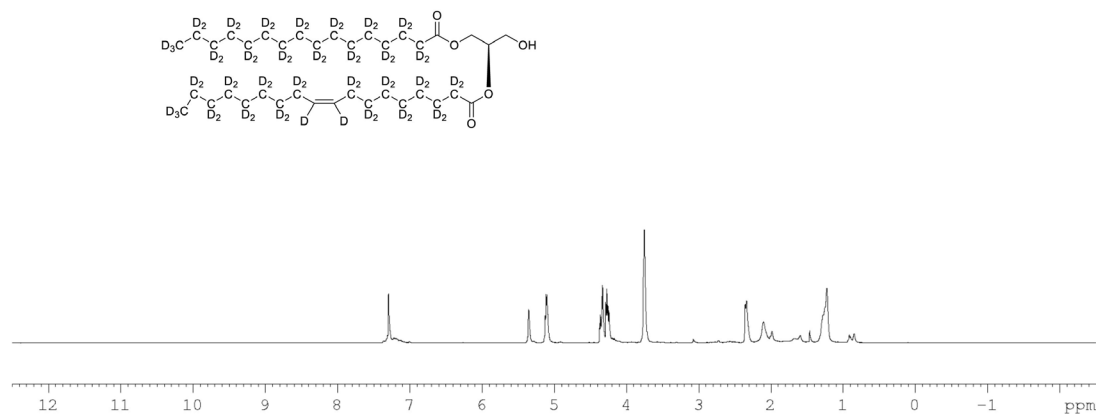
Appendix 1—figure 6. ^1H NMR of 1-palmitoyl- d_{31} -2-oleoyl- d_{33} -sn-3-benzyloxy-glycerol (**Appendix 1—figure 1**, molecule 3) in CDCl_3 . (400 MHz, CDCl_3), δ 0.82 (m, 6D), 1.19 (m, 35.35D), 1.53 (m, 3.74D), 1.94 (m, 3.34D), 2.25 (m, 2.63D), 3.56 (m, 1.71D), 4.27 (m, 1.04D), 5.35 (m, 1.92).



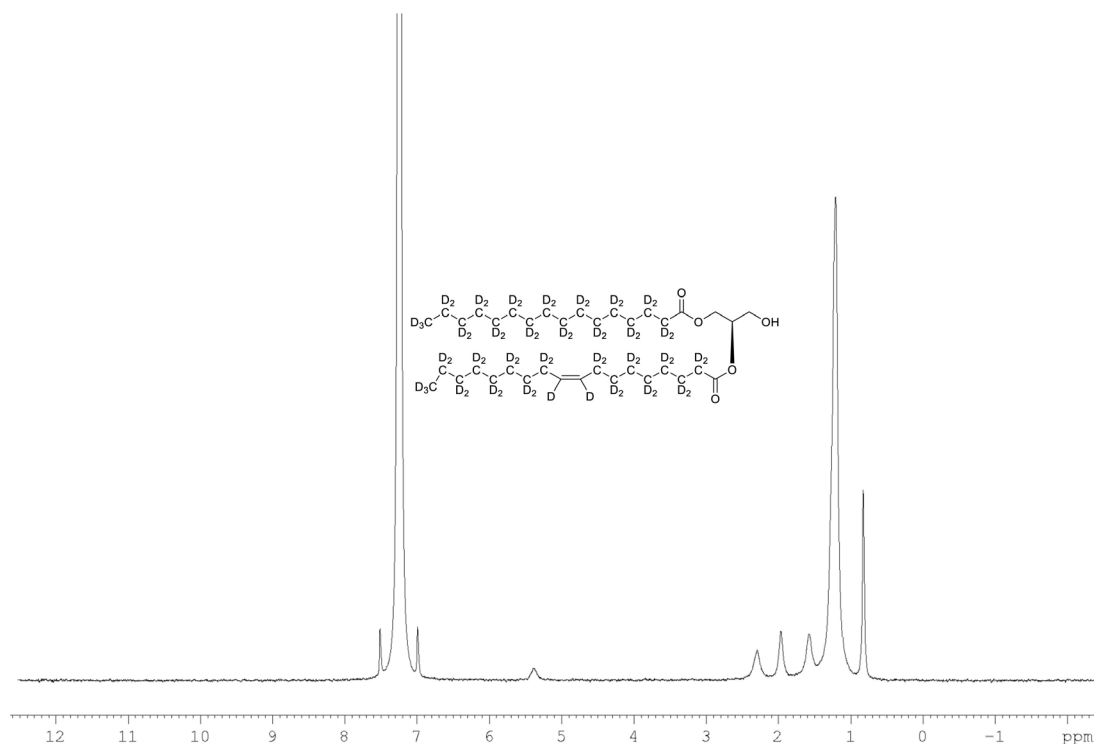
Appendix 1—figure 7. ^{13}C NMR of 1-palmitoyl- d_{31} -2-oleoyl- d_{33} -sn-3-benzyloxy-glycerol (**Appendix 1—figure 1**, molecule 3) in CDCl_3 . (400 MHz, CDCl_3), δ 13.08 (m), 21.60 (m), 23.96 (m), 26.50 (m), 28.2 (m), 30.60 (m), 33.80 (m), 62.60, 68.39, 70.10, 73.1, 127.7, 127.9, 128.5, 137.7, 173.1, 173.4.



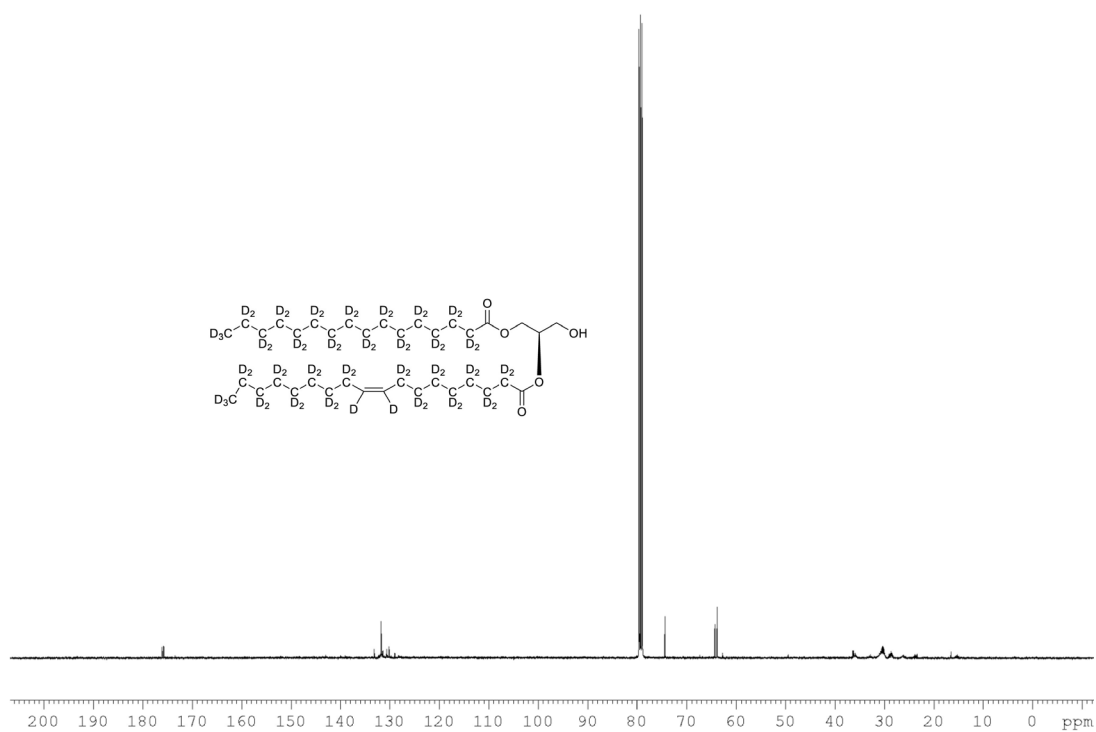
Appendix 1—figure 8. ESI-MS, m/z 749 [M^{+1}]⁺ of POPC precursor 1-palmitoyl-2-oleoyl-sn-benzyloxyglycerol- d_{64} (**Appendix 1—figure 1**, molecule **3**). Overall 94%D, isotope distribution d_{64} , 7.8%, d_{63} , 15.1%, d_{62} , 19.5%, d_{61} , 18.0%, d_{60} , 13.1%, d_{59} , 10.2%, d_{58} , 6.5%, d_{57} , 3.9%, d_{56} , 2.7%.



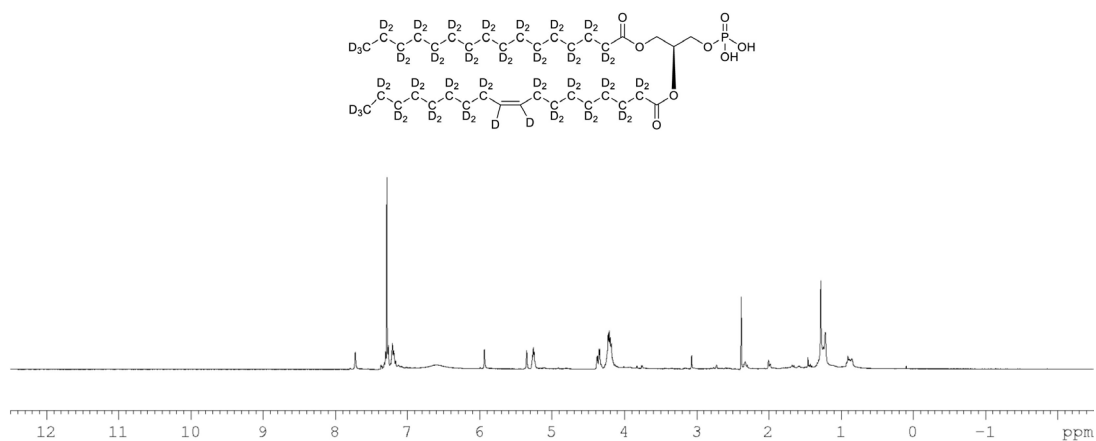
Appendix 1—figure 9. ^1H NMR of 1-palmitoyl- d_{31} -2-oleoyl- d_{33} -sn-3-glycerol (**Appendix 1—figure 1**, molecule **4**) in CDCl_3 . (400 MHz, CDCl_3), δ residual protons 0.24 (m, 0.47 H), 1.28 (m, 1.51 H), 1.67 (m, 2.24 H), 2.13 (m, 0.52 H), 2.23 (m, 1.29 H), 3.72 (m, 2 H), 4.30 (m, 2 H), 4.30 (m, 2 H), 5.10 (m, 1 H), 5.34 (s, 0.48 H).



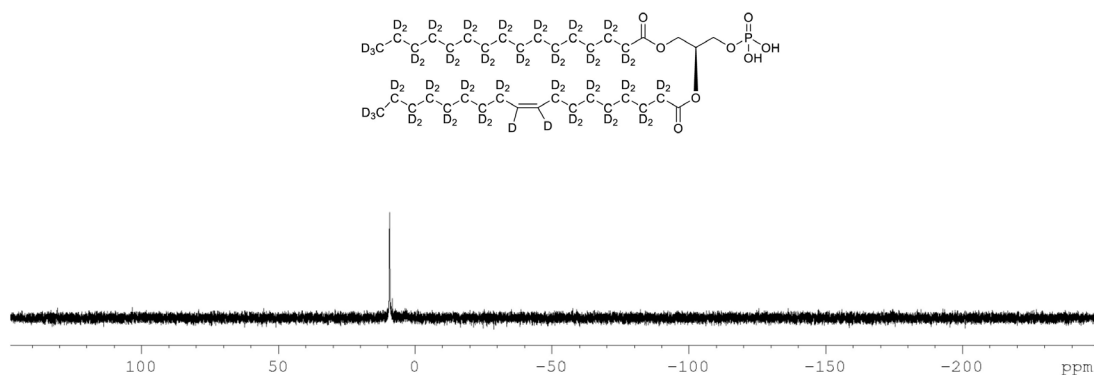
Appendix 1—figure 10. ^2H NMR of 1-palmitoyl- d_{31} -2-oleoyl- d_{33} -sn-3-glycerol (**Appendix 1—figure 1**, molecule 4) in CDCl_3 . (400 MHz, CDCl_3), δ 0.82 (m, 8.6D), 1.19 (m, 49.2D), 1.55 (m, 4.8D), 1.94 (m, 3.46D), 2.28 (m, 3.82D), 5.38 (m, 1.1D).



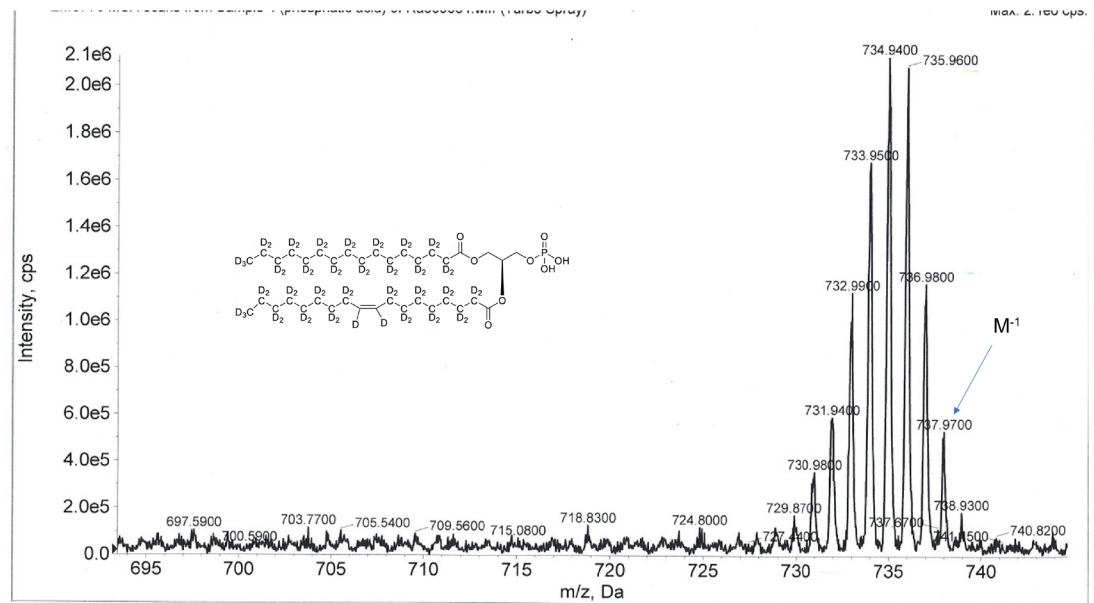
Appendix 1—figure 11. ^{13}C NMR of 1-palmitoyl- d_{31} -2-oleoyl- d_{33} -sn-3-glycerol (**Appendix 1—figure 1**, molecule 4) in CDCl_3 . (400 MHz, CDCl_3), δ 12.89 (m), 21.39 (m), 22.6 (m), 24.00 (m), 26.25 (m), 28.2 (m), 30.49 (m), 33.86 (m), 65.00, 60.76, 61.60, 71.64, 128.02, 129.14, 129.5, 173.53, 173.93.



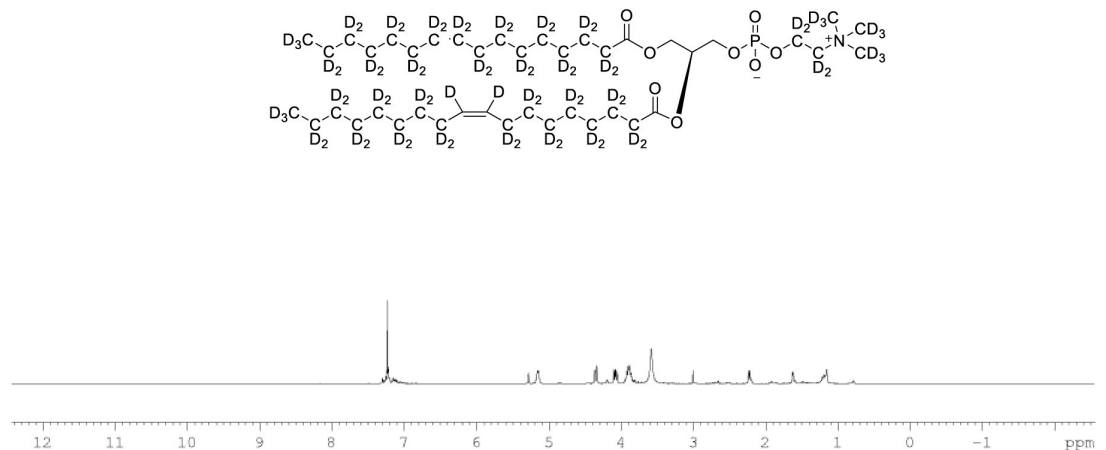
Appendix 1—figure 12. ¹H NMR of crude product 1-palmitoyl-d₃₁-2-oleoyl-d₃₃-sn-3-glycero-phosphatidic acid (**Appendix 1—figure 1**, molecule 5) in CDCl₃. This synthesised crude dried product was used in next step without further purification.



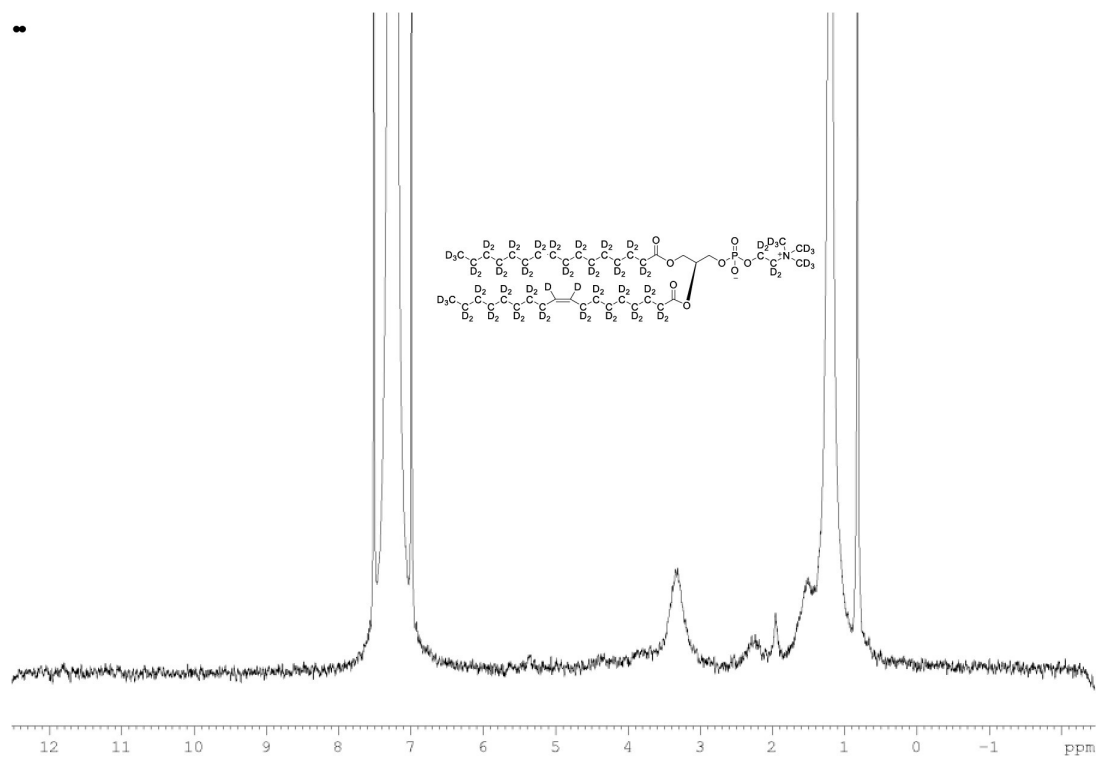
Appendix 1—figure 13. ³¹P NMR of crude product 1-palmitoyl-d₃₁-2-oleoyl-d₃₃-sn-3-glycero-phosphatidic acid (**Appendix 1—figure 1**, molecule 5) in CDCl₃. This synthesised crude dried product was used in next step without further purification.



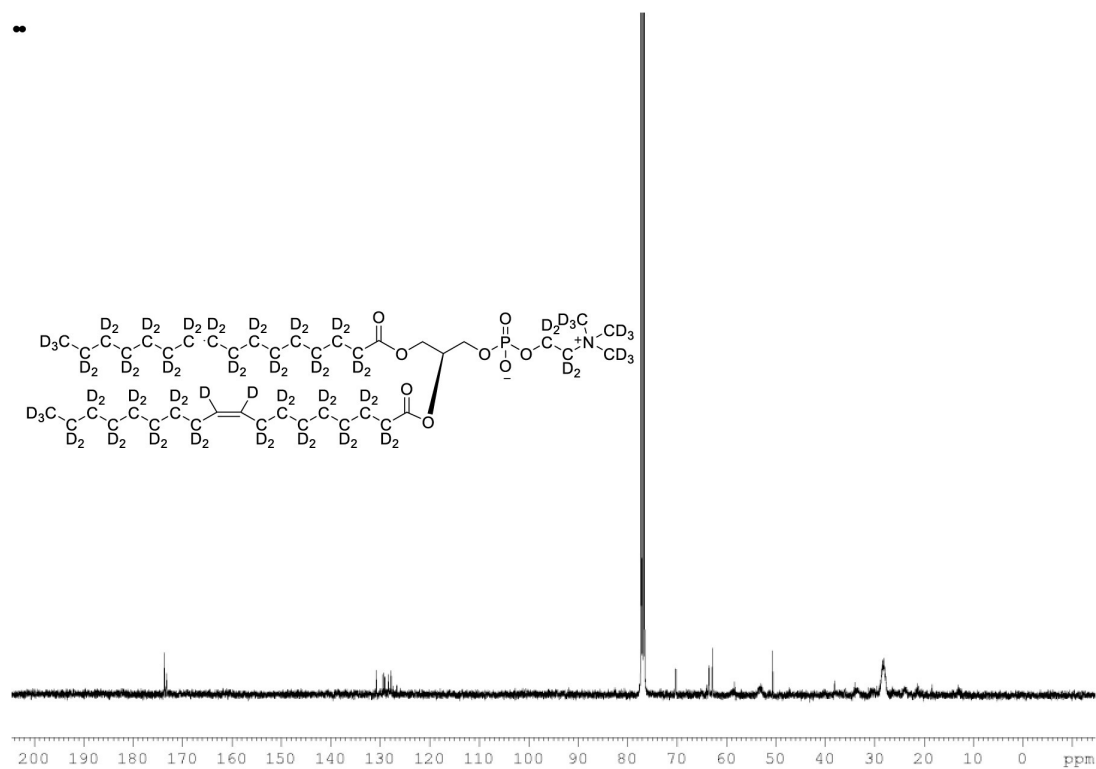
Appendix 1—figure 14. ESI-MS, m/z 737 [$M-1$] of crude product of 1-palmitoyl- d_{31} -2-oleoyl- d_{33} -sn-3-glycero-phosphatidic acid (**Appendix 1—figure 1**, molecule 5). Overall 94%D, isotope distribution d_{64} , 0.6%, d_{63} , 8.9%, d_{62} , 18.8%, d_{61} , 25.1%, d_{60} , 20.6%, d_{59} , 13.0%, d_{58} , 7.5%, d_{57} , 5.2%, d_{56} , 0.2%, d_{55} , 0.1%.



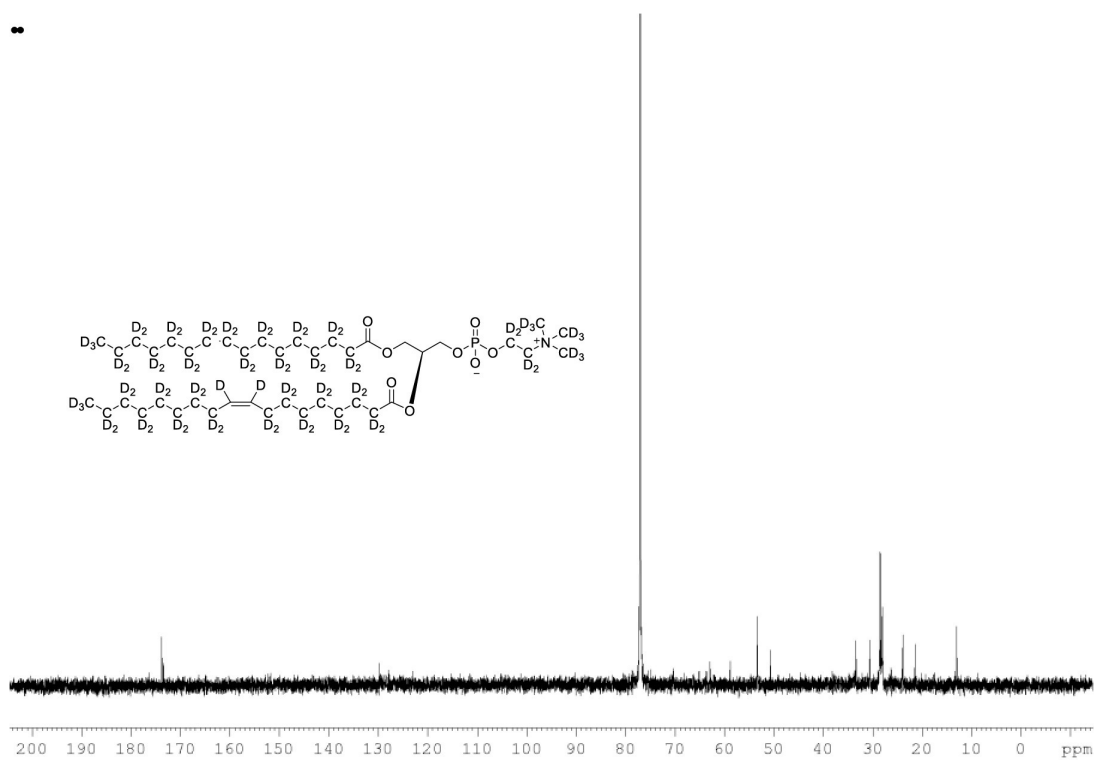
Appendix 1—figure 15. ^1H NMR of POPC- d_{77} in CDCl_3 , (400 MHz, CDCl_3), δ residual protons 0.85 (m, 0.17 H), 1.25 (m, 1.48 H), 1.54 (m, 0.22 H), 1.97 (m, 0.18 H), 2.22 (m, 0.66 H), 3.89 (m, 2 H), 4.08 (m, 1 H), 4.34 (m, 1 H), 5.14 (m, 1 H), 5.27 (s, 0.43 H).



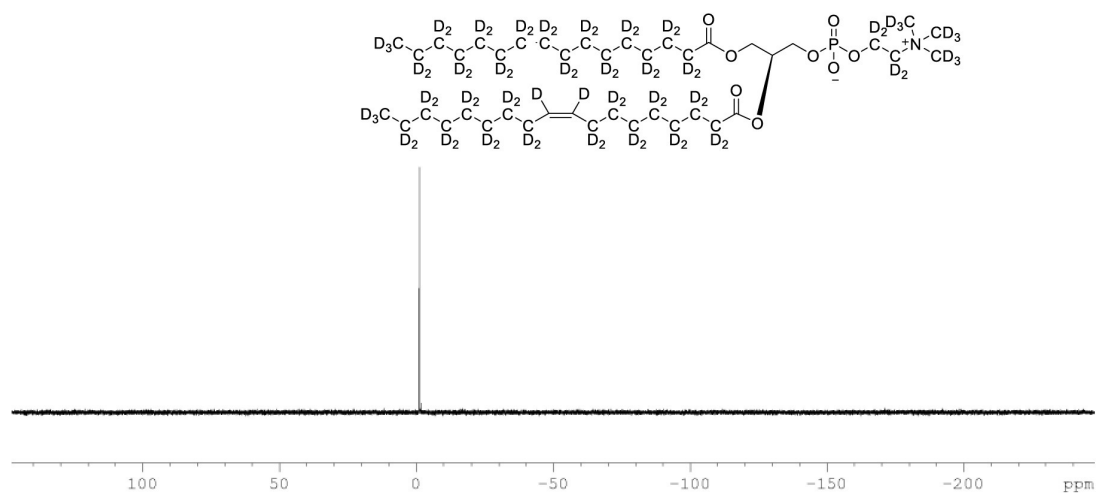
Appendix 1—figure 16. ^2H NMR of POPC- d_{77} in CDCl_3 . (400 MHz, CDCl_3), δ 0.80 (m), 1.19 (m), 2.20 (m), 1.93 (m, 6.0D), 3.35 (m), 3.84 (m), 5.36 (m).



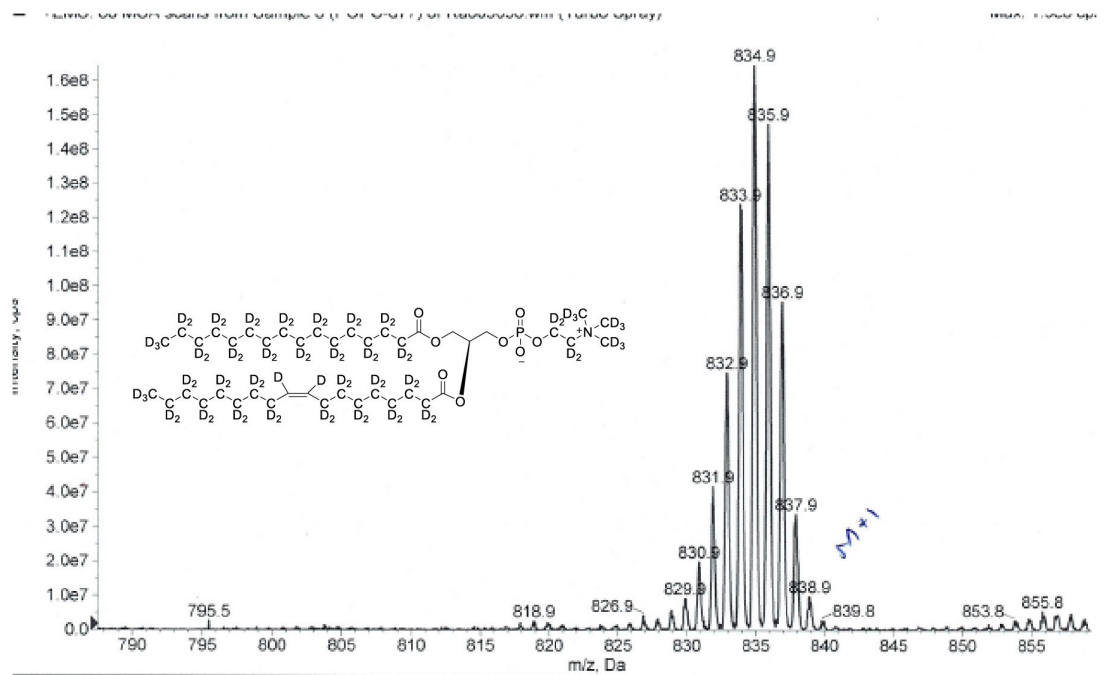
Appendix 1—figure 17. ^{13}C NMR of POPC- d_{77} in CDCl_3 . (400 MHz, CDCl_3), δ 13.03 (m), 21.48 (m), 23.88 (m), 26.24 (m), 28.36 (m), 30.49 (m), 33.72 (m), 53.17, 58.76 (m), 62.24 (m), 69.84 (m), 127.90 (s), 129.5, 173.31, 173.69.



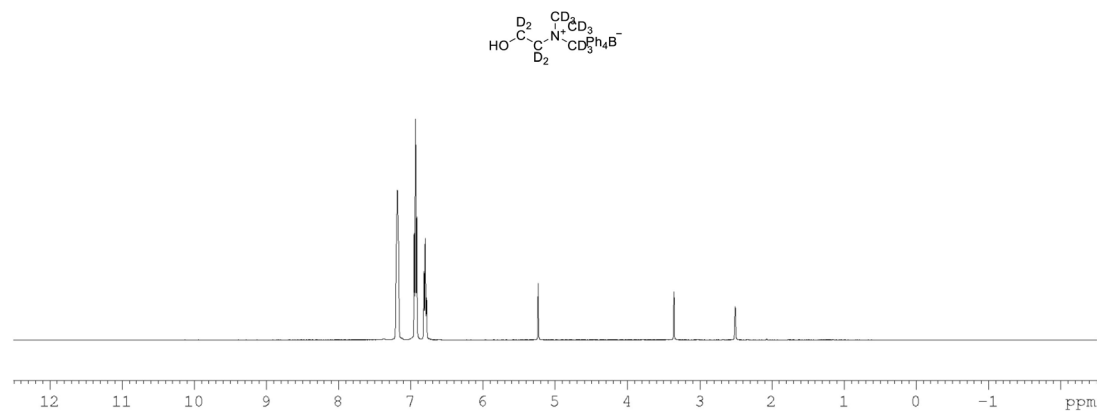
Appendix 1—figure 18. $\{^1\text{H}\}$ and $\{^2\text{H}\}$ decoupled ^{13}C NMR spectra of POPC- d_{77} in CDCl_3 .



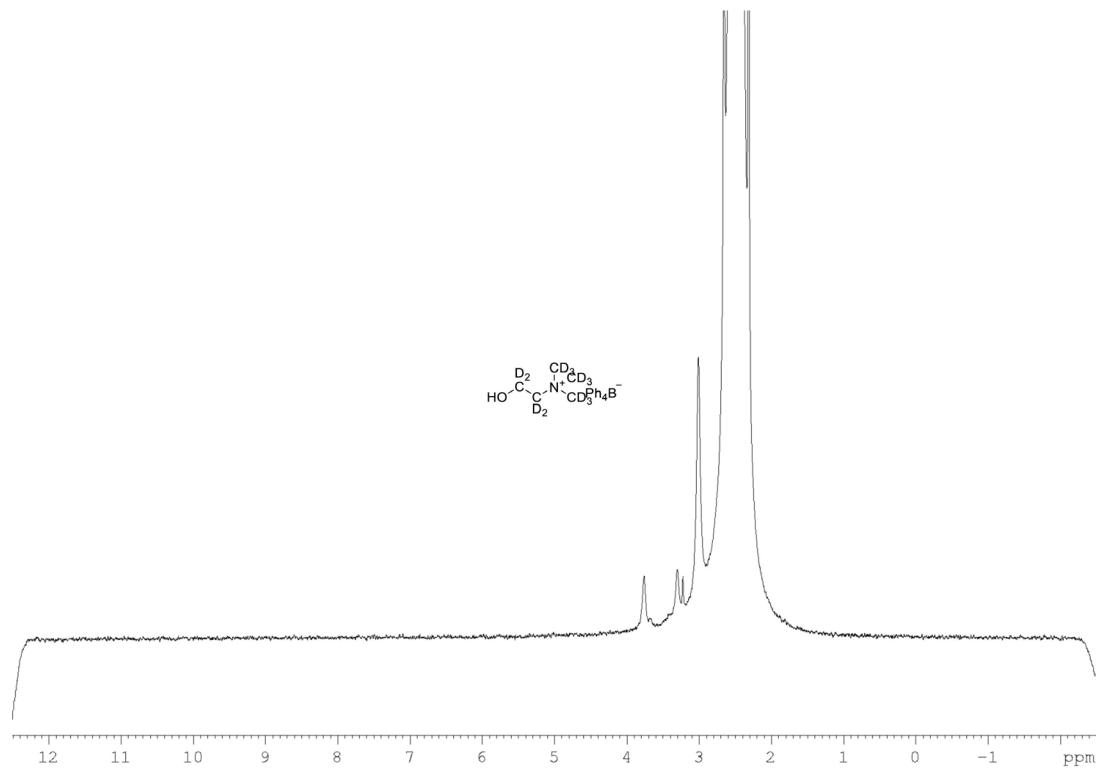
Appendix 1—figure 19. ^{31}P NMR of POPC- d_{77} in CDCl_3 . (400 MHz, CDCl_3), single peak at $\delta -2.20$.



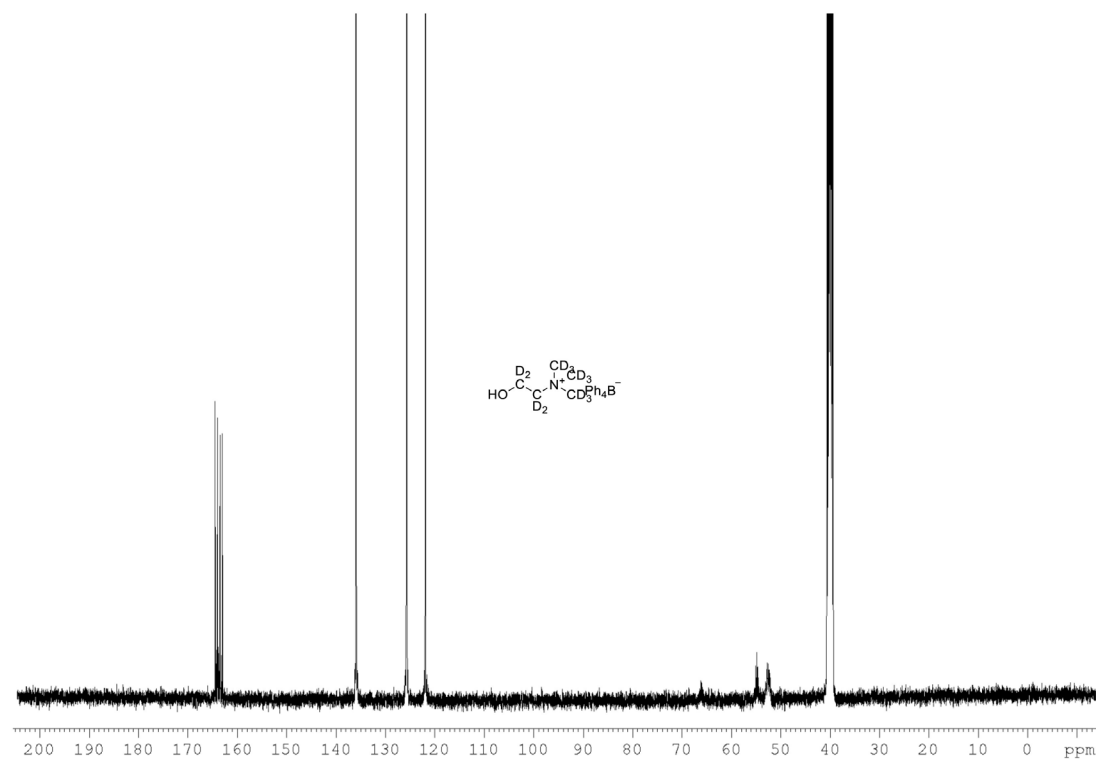
Appendix 1—figure 20. ESI-MS, m/z 838 $[M^{+1}]^+$ of POPC- d_{77} . Overall 93%D, isotope distribution d_{77} , 0%, d_{76} , 0%, d_{75} , 7.5%, d_{74} , 21.2%, d_{73} , 28.7%, d_{72} , 25.3%, d_{71} , 15.5%, d_{70} , 10.8%.



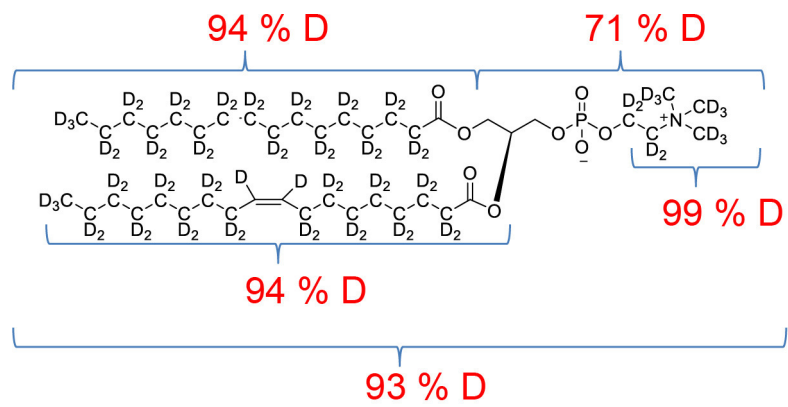
Appendix 1—figure 21. ^1H NMR of choline- d_{13} tetraphylborate (**Appendix 1—figure 1**, molecule 8) in DMSO- d_6 . (400 MHz, DMSO- d_6) δ 6.85 (m, 4 H), 6.96 (m, 8 H), 7.21 (m, 8 H).



Appendix 1—figure 22. ^2H NMR of choline- d_{13} tetraphylborate (**Appendix 1—figure 1**, molecule **8**) in DMSO-d_6 . (61.4 MHz, DMSO-d_6) δ 3.30 (m, 9D), 3.32 (m, 2D), 3.78 (m, 2D).



Appendix 1—figure 23. ^{13}C NMR of choline- d_{13} tetraphylborate (**Appendix 1—figure 1**, molecule **8**) in DMSO-d_6 . (100 MHz, DMSO-d_6) δ 52.5 (m), 54.9 (m), 121.9, 125.9, 136.2, 163.9 (m).



Appendix 1—figure 24. POPC-d₇₇ percentage distribution of D levels at different sites.